CURRENTS OF THE 2011 TOHOKU TSUNAMI SOUTH OF OAHU, HAWAII, FROM HIGH-FREQUENCY DOPPLER RADIO SCATTEROMETER

A THESIS SUBMITTED TO THE GRADUATE DIVISION OF THE UNIVERSITY OF HAWAIʻI AT MĀNOA IN PARTIAL FULFILLMENT OF THE REQUIREMENTS FOR THE DEGREE OF

MASTER OF SCIENCE

IN

OCEANOGRAPHY

AUGUST 2014

By

Lindsey R. Benjamin

Thesis Committee:

Pierre Flament, Chairperson
Douglas Luther
Kwok Fai Cheung

Keywords: currents, tsunami, model validation

ABSTRACT

A 16-MHz high-frequency Doppler radio scatterometer (HFDRS) deployed on the south shore of Oahu, Hawaii, detected oscillatory radial currents following the 2011 Tohoku tsunami. Observational data on tsunami currents over a two-dimensional area provided an opportunity to validate the currents and their spatial patterns in a non-hydrostatic wave model of the tsunami from its generation to the shores of the Hawaiian Islands. Over Penguin Bank, a 50-m bank extending west from Molokai, currents were split into two distinct areas, with stronger, longer period currents that persisted longer on the south part of the bank (0.27 ms^{-1} currents at 43 min lasting 6 hours versus 0.14 ms^{-1} currents at 27 min lasting 2 hours). The EOF spatial maps suggested that standing half-wave and full-waves in sea level formed over the bank. Modeled currents over Penguin Bank were similar to observations, but with the north-south asymmetry less pronounced. In the near-shore, along-shore observations showed a long-period current oscillating at 43 min that stretched the entire coastline, while modeled currents showed strong evidence for edge waves. EOF analysis of the near-shore revealed that the HFDRS and model showed different processes. Despite HFDRS data issues with azimuthal side lobe contamination and decreased angular resolution at high steering angles, the spatial comparison between observations and model currents were encouraging for a first attempt at two-dimensional model validation of tsunami currents.

TABLE OF CONTENTS

LIST OF TABLES

LIST OF FIGURES

LIST OF ABBREVIATIONS AND SYMBOLS

Abbreviations

ADC	Analog-to-Digital Converter
ADCP	Acoustic Doppler current profiler
DART	Deep-ocean Assessment and Reporting of Tsunamis
DDS	Direct digital synthesizer
E	Eigenvector
EOF	Empirical Orthogonal Function
FIR	Finite Impulse Response, a type of digital filter
FMCW	Frequency-Modulated Continuous Wave
FT	Fourier Transform
HFDRS	High-frequency Doppler radio scatterometer
KAL	Kalaeloa site
KOK	Koko Head site
LO	Local Oscillator
Mw	Moment-magnitude
NEOWAVE	Non-hydrostatic evolution of ocean wave
NJAP	National Police Agency of Japan
PA	Power Amplifier
PB	Penguin Bank
PTWC	Pacific Tsunami Warning Center
RMSE	Root-mean-square error
Rx	Receive
Tx	Transmit
UTC	Universal Coordinated Time

Units

dB	Decibel
dBm	Decibel-milliwatt
h	Hour
kHz	Kilohertz
km	Kilometer

m	Meter
MHz	Megahertz
min	Minute
s	Second

Symbols

B	Tx chirp bandwidth
c	Speed of light in a vacuum
d	Rx antenna spacing distance
D	Rx antenna array length
D_a	Diameter of the circular lens of a telescope
E	Energy
f	Ocean wave frequency
F_c	Tx center frequency
F_E	Energy flux
δF_r	Change in frequency due to travel time in a chirp
g	Gravitational acceleration at Earth's surface
H	Ocean wave amplitude
h	Ocean depth
I	Signal intensity
I_0	Base signal strength
j	Number of points of comparison, number of time steps in EOF analysis
k	Ocean wavenumber
K_E	Kinetic energy
l	Ocean wavelength
L	Radio wavelength of F_c
m	Mass (general)
n	Number of antennas in Rx array
N	Order of scattering
p	Ocean wave period
δr	Range resolution

r_{max}	Maximum range of HFDRS
$RMSE$	Root-mean-square error
t	Time
δt	Temporal resolution, also integration time
T_c	Time period of a single Tx chirp
δT	Total Tx/Rx signal travel time
u	Water particle/current velocity
δu	Current velocity resolution
U	Potential energy
v	Velocity (general)
v_g	Ocean wave group speed
v_p	Ocean wave phase speed
w	Difference in signal travel distance due to α or $\beta \neq 0$
α	Radio wave incident angle measured from normal to the array
β	Beam steering angle measured from normal to the array
$\delta\beta$	Angular frequency of beamforming
γ	Bragg scattering angle in classical Bragg scattering
ζ	Ocean wave orbit semi-minor axis
η	Sea surface level
θ	Ocean modulation of Rx signal
$\delta\theta$	Frequency resolution of ocean modulation, related to velocity resolution
λ	Eigenvalue
Λ	Tx signal wavelength in classical Bragg scattering
ξ	An EOF mode
ρ	Water density
φ	Phase shift from Tx to Rx
$\delta\varphi$	Frequency resolution of range
ψ	Fourier transform
$\lvert\psi^2\rvert$	Spectral amplitude
ω	Ocean wave angular frequency

$\mathfrak{I}$	Imaginary part of a complex number
$\mathfrak{R}$	Real part of a complex number

CHAPTER 1
INTRODUCTION

1.1 2011 Tohoku Tsunami

On 11 March 2011 at 0546 UTC, a moment-magnitude (M_w) 9.0 earthquake struck Japan, with an epicenter 140 km east of Sendai and 373 km northeast of Tokyo [Figure 1.1]. The megathrust earthquake, which involved a 200-km long section of the Eurasian plate sliding 60 m along a 10° incline over the slowly subducting Pacific Plate, generated a large tsunami [Appendix A]. The closest sea level measurement to the epicenter, the Deep-ocean Assessment and Reporting of Tsunamis buoy (DART) buoy 21418, recorded a 1.75 m tsunami wave height in 4000 m of water. The near-field tsunami devastated the northeast coast of the island of Honshu in Japan, with a maximum run-up of 39.7 m at Miyako and an inundation greater than 5 km on the Sendai Plain [Mori et al., 2011]. Nearly 16000 people were killed, and almost 3000 are still missing [National Police Agency of Japan]. The tsunami also resulted in a disaster at the Fukushima nuclear power station, and the total damage in Japan is an estimated $156–$244 billion [Mimura et al., 2011].

Though nowhere near as devastating as the near-field tsunami, the far-field tsunami also caused damage around the Pacific. The Pacific Tsunami Warning Center (PTWC) in Ewa Beach, Hawaii, initiated a tsunami warning for Japan and its immediate surroundings (and a watch for the rest of the Pacific) at 0555 UTC that was upgraded to a Pacific-wide tsunami warning at 0730 UTC. In the Kuril Islands, a building was flooded and some ice was deposited on beaches, which double as roads [Kaistrenko et al., 2013]. In New Zealand, several harbors and vessels suffered minor damage [Borrero et al., 2013]. In the Galapagos Islands, several buildings and coastal properties were flooded [Lynett et al., 2013]. There was some damage along the West Coast of the United States, particularly in harbors, where even small wave amplitudes can cause swift currents that damage or destroy vessels and harbor facilities [Allan et al., 2012]. In Hawaii, over 200 small vessels in Keehi Lagoon Marina were damaged by strong currents, as were some dock facilities; total damage in Hawaii was an estimated $30 million [Dunbar et al., 2011]. Additionally, the Coast Guard prevented vessels from returning to some areas for a time because of strong currents.

1.2 Tsunami Currents

The majority of the damage in Hawaii was caused by strong currents, as was that along the West Coast of the United States. Despite the dangers posed by tsunami currents, they are rarely studied, even in models. Tsunami currents in the field are difficult to measure because the unpredictable generation of

tsunamis prevents the easy deployment of current meters to study them. Fortuitous detection of tsunami currents with acoustic Doppler current profilers (ADCPs) can and has allowed point validation of modeled currents [Yamazaki et al., 2012; Cheung et al., 2013], but there has been no two-dimensional spatial validation.

High-frequency Doppler radio scatterometer (HFDRS) can map surface currents over an area [Appendix B] and could potentially be used to validate spatial current patterns in tsunami models. HFDRS measures the ocean current radial to the instrument averaged over a volume of water at the surface that spreads 0.5–5 km in range, 1–11° in angle, and 0.5–2 m in depth, depending on operational parameters. The areal dimensions of the HFDRS measurement-volume are small relative to the long wavelength of a tsunami, so the velocity of water particles within the volume in tsunami wave orbits is homogeneous and appears as a current. The relatively low velocity resolution of HFDRS at high temporal resolution (0.074 ms^{-1} at 4.2 min for 16.3 MHz center frequency transmit signal) does require that the currents be very strong. Shoaling of a wave causes an increase in water particle velocity [Appendix A], so tsunami currents are best detected by HFDRS in shallow water. Shallow areas, especially near the coast, may exhibit signs of resonance phenomenon if energy is trapped in the region, so HFDRS can also detect the resonant response to the tsunami.

The 2011 Tohoku tsunami has been detected by HFDRS in Chile [Dzvonkovskaya et al., 2011], in California and Hokkaido [Lipa et al., 2011], and in the Kii Channel in Japan [Hinata et al., 2011]. The continental shelf in Chile was too close to the coast to allow the HFDRS to detect the tsunami early enough to provide much advanced warning, and the instrument was not positioned to view any coastal resonance modes that may have been excited (see Yamazaki et al. [2011b]). The same restrictions on viewing the spatial current patterns were present in Hokkaido and two of the three California HFDRS sites: the shallow area around the Bolinas, California, HFDRS could have allowed a spatial analysis of the resonant response to the tsunami, but one was not performed. The shallow areas of the partially enclosed Kii Channel would also have allowed for a detailed analysis of resonant currents, but again, this was not done. The spatial patterns of tsunami currents have not been analyzed in any HFDRS study, nor have any attempts been made to judge the potential contributions of HFDRS to two-dimensional model validation.

1.3 Opportunity in Hawaii

Hawaii provides an opportunity to detect currents from the 2011 Tohoku tsunami, analyze the spatial structure of the resulting resonance, and validate the two-dimensional patterns of modeled currents excited in the area. There was an HFDRS operational on the eastern end of Oahu's south shore during the

event that included shallow Penguin Bank and along-shore currents in its coverage area. The HFDRS was deployed to monitor low-frequency currents south of Oahu, but the inclusion of areas of shallow bathymetry in its coverage area can also allow it to detect tsunamis. Tsunami currents alone are not expected in the area because of both the complex arrival of the initial tsunami wave front [Song et al., 2012], as well as the physical separation of the shallow areas under observation. Instead, the resonant response to the tsunami arrival and subsequent trapping of tsunami energy in the Hawaiian Islands is anticipated. Previous modeling studies of tsunami responses in the Hawaiian Islands, American Samoa, and along the Chilean coastal shelf show a strong, prolonged, and complex resonant response that depends less on the characteristics of the individual tsunami and more on the natural resonant modes of the area [Munger and Cheung 2008, Roeber et al., 2010, Yamazaki and Cheung 2011]. Several of these modes in Hawaii have strong antinodes over Penguin Bank or along Oahu's south shore [Figure 1.2], within the coverage area for the HFDRS. The location of the maximum of total spectral amplitude coincides with Penguin Bank, making its inclusion in the coverage area very useful as it may act as a probe for what occurs around the islands.

Hawaii's past history with tsunamis has made the study of them important for civil safety reasons. Adding that to scientific interest, tsunami modeling is an area of active research in Hawaii. Several tsunamis, including the 2011 Tohoku tsunami, have been modeled in the region. There is an opportunity not only to compare modeled currents during the 2011 Tohoku tsunami to those measured by HFDRS, but also to evaluate the potential of HFDRS as a tool for two-dimensional validation of modeled currents.

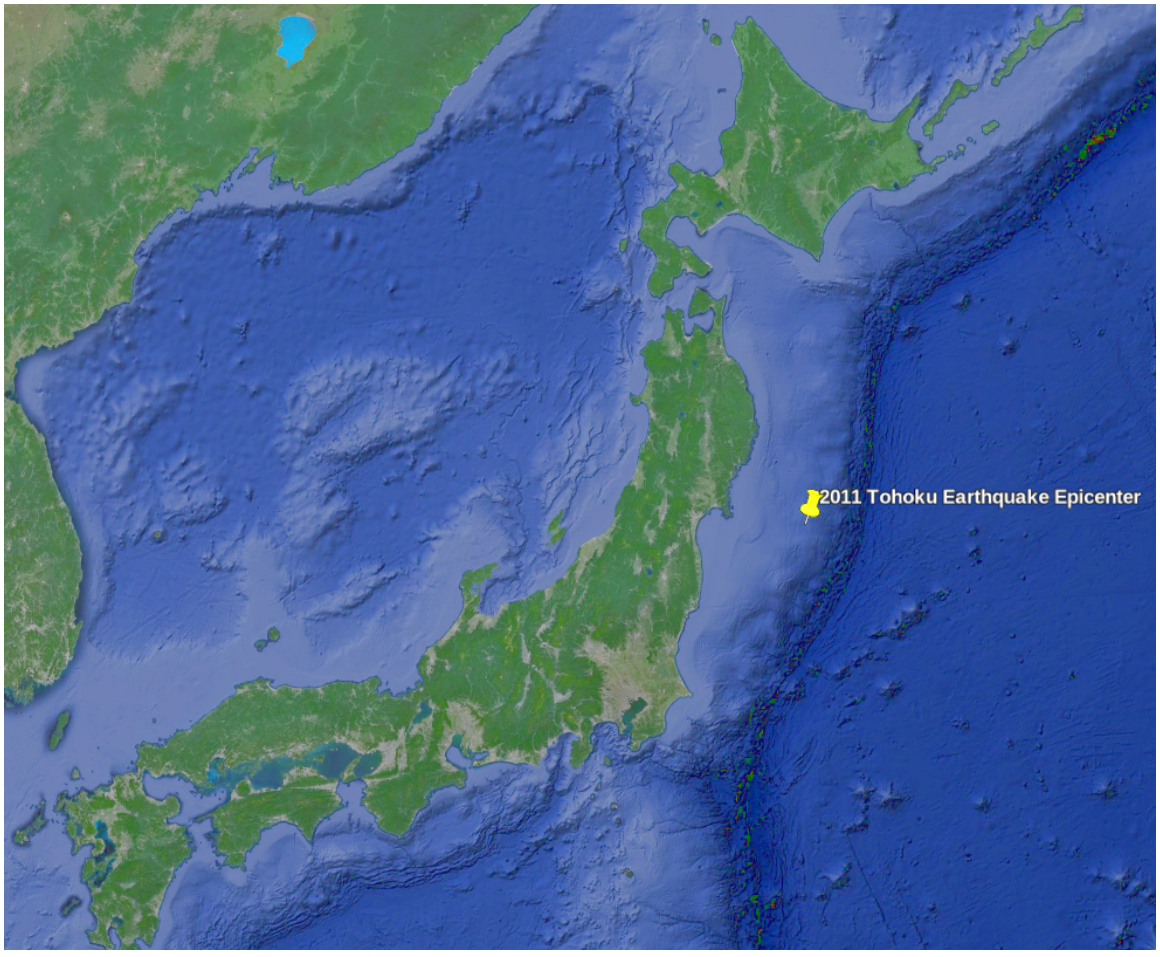

Figure 1.1. Map of Japan and the surrounding area, with the epicenter of the earthquake that triggered the 2011 Tohoku tsunami marked.

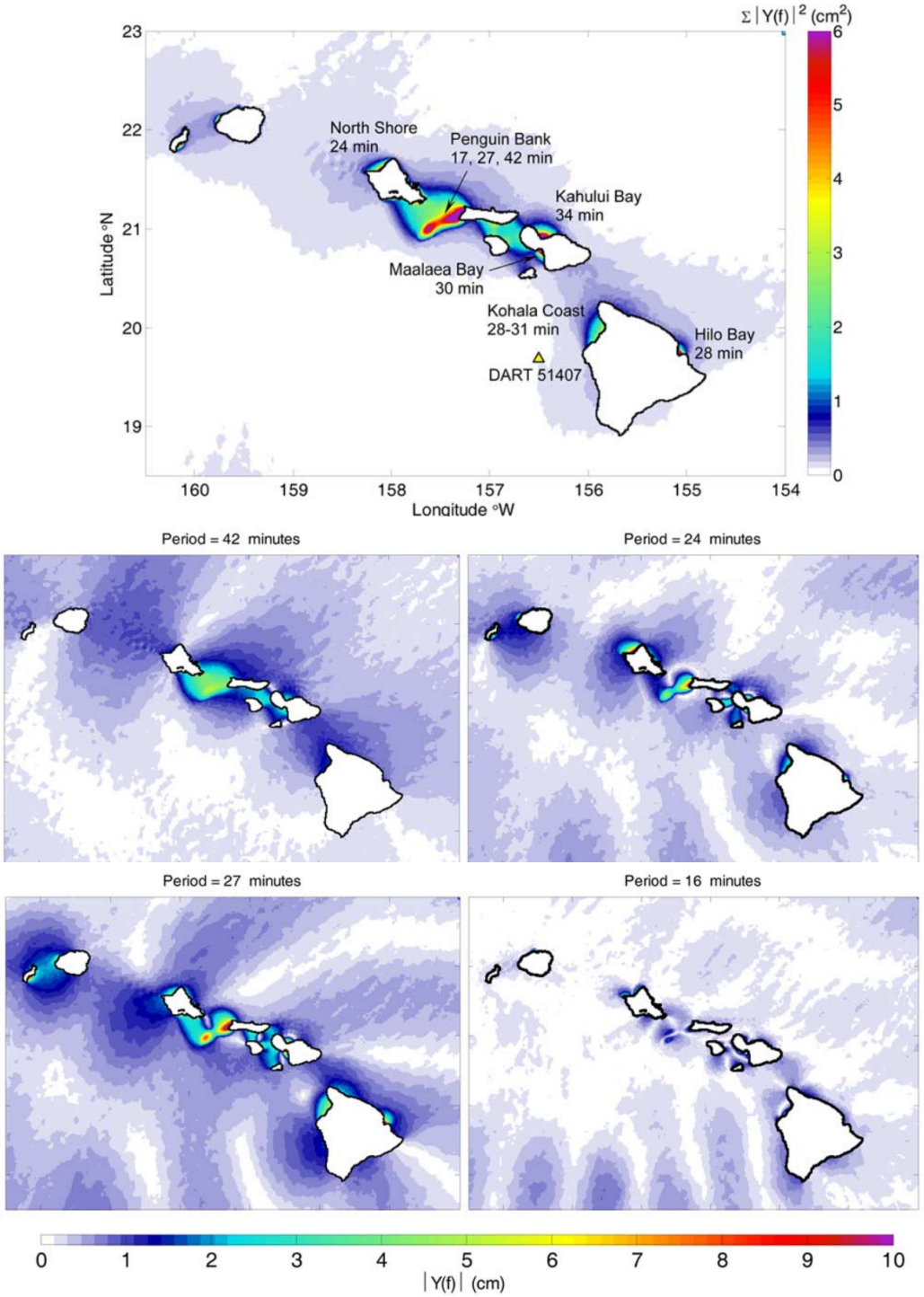

Figure 1.2. Total spectral amplitude (top panel) and spectral amplitude for certain periods (bottom panels) across the Hawaiian Islands from modeling the 2006 Kuril Islands Tsunami. From Munger and Cheung [2008], Figures 2 and 4.

CHAPTER 2
DATA AND METHODS

2.1 HFDRS Data

The HFDRS at Koko Head, or the KOK HFDRS, was in operation on Oahu's south shore during the 2011 Tohoku tsunami [Figures 2.1, 2.2]. It operated at 16.13 MHz with a bandwidth of 100 kHz. Included in its coverage area is Penguin Bank and most of the south shore west of the site. The range of KOK was about 100 km [Appendix B]. Only 11.2 min of data with 2048 chirps were gathered in every 15 min. The KOK HFDRS data was reprocessed with 768 chirps per half-overlapping 4.2 min period, giving a temporal resolution of 2.1 min and a Doppler resolution of 0.074 ms^{-1} [Appendix B]. The spatial resolution was 1.5 km in range and 11° in azimuth. KOK has 121 angular cells and 54 range cells available, with 96% data available between 1300 UTC on 11 March 2011 and 0100 UTC on 12 March 2011. Missing data points in space or time were interpolated. A mask was applied to remove data points too close to the coast. A low-pass finite impulse response (FIR) filter with a 3 dB cutoff at 8 min was applied to all HFDRS data to smooth the noise, while a high-pass FIR filter with a 3 dB cutoff at 200 min was applied to remove the tides and other lower frequency motions (e.g., inertial motion, Kelvin waves) [Appendix C]. Current values have an uncertainty of 0.03 ms^{-1} [Appendix D].

2.2 Model Data

The NEOWAVE (Non-hydrostatic Evolution of Ocean Wave) model, developed by Yamazaki et al. [2009, 2011a] was used to model the 2011 Tohoku tsunami from its generation at the earthquake source near Japan to the coastlines of Hawaii. The model utilizes dynamic sea floor deformation at the source which influences energy transfer and subsequent wave formation. Because it includes a non-hydrostatic pressure term and a shock-capturing scheme, it is possible to model weakly dispersive waves and flow discontinuities such as bores and hydraulic jumps, which can have significant effects on modeled run-up. The inclusion of depth-dependent Gaussian topographic smoothing is important because it minimizes the smoothing of features in shallow water, where the bathymetry is most important in determining the characteristics of the waves. The 2011 Tohoku tsunami modeled with NEOWAVE has been validated at basin and coastal scales using DART buoys, tide gauges, bottom-mounted pressure sensors, and ADCPs [Yamazaki et al., 2011b; Yamazaki et al., 2012; Cheung et al., 2013]. Modeled, depth-integrated currents for the HFDRS coverage areas were taken from the same run utilized in the model's validation. The model's arrival time as measured by the first arriving peak was ~6 min late

relative to the HFDRS. Late arrivals are normal in tsunami modeling because variations in water density and the elasticity of the Earth are not taken into account [Tsai et al., 2013, Watada 2013]. The whole model data set was shifted 6 min to account for this difference. Modeled data was re-gridded from 1-min, 24 arc second resolution to match the spatial and temporal sampling of the KOK HFDRS to enable a precise comparison between model and HFDRS. The same FIR filtering scheme used on the HFDRS currents was used on the model currents.

2.3 Sea Level Data

Though the purpose of this work is to compare currents, sea level measurements from the Honolulu tide gauge, located in Honolulu harbor, and DART 51407, located ~225 km southeast of Honolulu [Figure 2.1], are used briefly to set the scene of the tsunami's arrival in Hawaii. All data is taken at one-min sampling interval. For these sites, there was 98% and 97% of the time between 1300 UTC on 11 March 2011 and 0100 UTC on 12 March 2011 for Honolulu tide gauge and DART 51407 data, respectively. All sea level data sets were subject to the same FIR filtering scheme as the current data.

2.4 Spectral Analysis

Fourier transforms were performed with zero-padded, windowed time-series. The squared spectral amplitudes were smoothed by averaging adjacent bins, every other energy bin being independent. Spectral phases were determined by the argument of the original Fourier transform [Appendix C].

2.5 EOF Analysis

Empirical orthogonal function (EOF) analysis was performed to find spatial modes and their temporal series. The EOF maps were normalized to maximum magnitude of 1, and their time series were scaled by multiplying by the normalization constant and by the fraction of variance explained by that EOF, to convert the units to current speed in ms^{-1}.

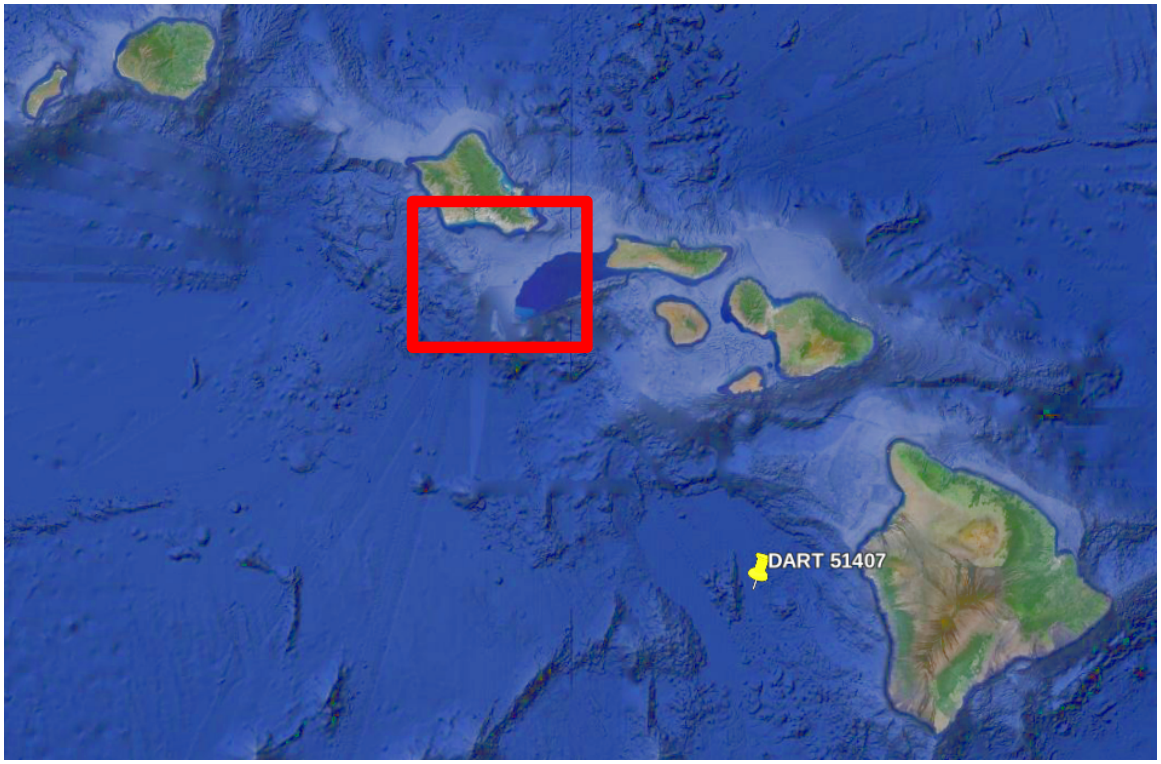

Figure 2.1. Map of the Hawaiian Islands showing the location of DART buoy 51407 west of Hawaii Island. The area within the red box is the main study area.

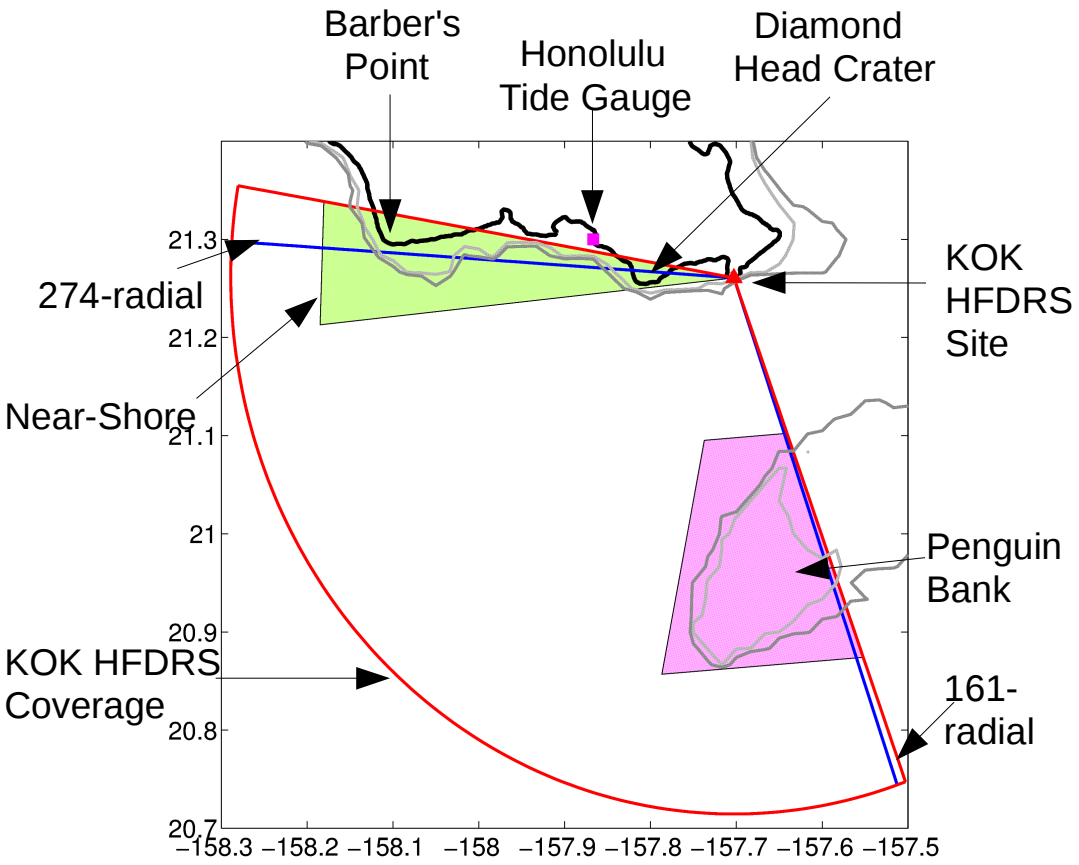

Figure 2.2. Map of main study area showing south Oahu, 50- and 100-m isobaths (grey lines), the KOK HFDRS site (red triangle), the coverage of the KOK HFDRS (red lines), two radial Lines used in the study (161 at right, 274 near the top, both in blue), the location of the Honolulu tide gauge in Honolulu Harbor (purple square), two points of interest on the coast (Diamond Head Crater and Barber's Point), and two areas of interest sed in the study: the near-shore region in green, and the Penguin Bank region in pink. The shallow bathymetric feature on the right side of the coverage area is Penguin Bank.

CHAPTER 3
RESULTS

3.1 Sea Level

The first tsunami wave crest reached the area south of Oahu at 1317 UTC on 11 March 2011, with near-simultaneous arrivals at the Honolulu tide gauge and DART 51407 [Figure 3.1]. Strong energetic oscillations were observed in both data sets, though the response at the Honolulu tide gauge was nearly three times as strong as that of the DART buoy. The long-period oscillations at the Honolulu tide gauge continued with little damping for 5 h before they calmed significantly. The short-period oscillations had a smaller amplitude than the long-period waves, and they appeared to dampen more quickly. There were very few short-period oscillations present in the DART buoy data, and the long-period oscillations died around the same time as those at the Honolulu tide gauge. The peak periods of the oscillations of both sea level measurements were also different beyond a common 43-min peak, which is the strongest in both data sets. The Honolulu tide gauge showed smaller peaks at 9–11 min, 16 min, and 27 min. There were no strong peaks in the DART spectrum besides the 43-min peak.

3.2 Penguin Bank

The tsunami arrival is marked by the appearance of energetic oscillatory radial currents over Penguin Bank in both the HFDRS and the model, as seen in plots of radial velocity in 161º direction [Figure 3.2], representative of any radial that crosses Penguin Bank (PB). The KOK data shows north-south asymmetry over the bank in terms of current magnitude, as well as the duration of the currents; those on the southern part of the bank are stronger (from –0.27 to 0.19 ms^{-1} as opposed to –0.14 to 0.12 ms^{-1} on the northern part of the bank) and the oscillations last longer. Typical currents off the bank are -0.02 to 0.02 ms^{-1}. In the model, the northern and southern parts of the bank are not quite as isolated from one another (as seen in the crossing of energetic currents from one side to the other), and the asymmetry in strength and duration is not as prominent (–0.28 to 0.27 ms^{-1} on the southern part as opposed to –0.23 to 0.27 ms^{-1} on the northern part of the bank). The currents on the two parts of the bank are at least partially out of phase with one another in both the HFDRS and modeled data, indicating a possible coupling of the two areas.

The spatial averages of the radial currents along the 161° direction in the northern and southern Penguin Bank regions show that the strength and duration asymmetry is present in both the HFDRS and model [Figure 3.3]. There is good agreement between the modeled and HFDRS currents in the north bank for the first hour, but the HFDRS amplitude drops significantly after that and is then indistinguishable

from noise. The modeled currents continue to oscillate with roughly the same amplitude for 3 h before dying. The short length of time of good agreement relative to the length of the time series renders a comparison of spectra useless. The largest peak in the modeled currents is at 27 min, and that is about the period of the first two oscillations in the HFDRS data as well. For the south bank averaged currents, there is good agreement between the model and HFDRS in both period and amplitude for the entirety of the time shown. The 43-min spectral peaks agree quite well in spectral amplitude, but there are smaller peaks in the model spectrum at 13, 27, and 31 min that are absent in the HFDRS spectrum.

Spectral amplitudes for given periods show that Penguin Bank is a hot-spot of activity in both HFDRS and model data [Figure 3.4]. The north and south bank regions are separate and have distinct amplitude features for most periods, though for 63 min the whole bank is a single feature. HFDRS amplitudes on the north bank are weaker than on the south bank, but in the model they usually have comparable strength. All spectral phases [Figure 3.5], for which only patterns can be compared, show a distinct node across the center of the bank, with the exception of the 63-min phase, with a node south of the bank and a smooth phase transition across the crest of the bank.

The results of empirical orthogonal function analysis over Penguin Bank are shown in Figures 3.6 and 3.7; HFDRS modes up to mode 5 do not have significant errors, while in the model those up to mode 6 have small errors [North et al., 1982; Appendix D.3]. The EOF maps are similar enough between HFDRS and model to encourage further comparison. The first mode, which contains 65% of the variance for the HFDRS and 53% for NEOWAVE, shows long-period opposing radial currents on the north and south Penguin Bank regions, with those on the south bank being significantly stronger. The model has stronger north bank currents in this mode than the HFDRS. The phase and amplitude of the first EOF time series shows good phase and amplitude agreement between modeled currents and HFDRS currents. There are short-period components to the modeled EOF time series that are not present in the HFDRS time series, and these can also be seen in the spectra of the time series. The 43-min peaks in the spectra show good agreement. The second mode, with 9% of the HFDRS variance and 16% of the model variance, also has opposing currents on the north and south bank regions, but both areas of maximal amplitude are southwards of those in the first mode. Also, the north bank currents are stronger in this mode. The amplitudes and phases of the EOF time series do not agree, with the model being stronger than the HFDRS (by 0.02 ms^{-1}). The spectral peaks also do not line up, with the model having a much broader spectrum of periods than the HFDRS. For the third mode, with 5% of HFDRS variance and 11% of model variance, the EOF maps show strong currents on the north and south bank regions in the same direction,

with a region of oppositely-directed current in between them. For the HFDRS, the southern area of maximum amplitude is weaker, but for the model it is the middle area that is weaker. The amplitudes and phases in the EOF time series do not match for this mode, nor do the periods of oscillation.

3.3 Near-Shore

The arrival of the tsunami in the near-shore area was marked by the appearance of a long-period, wide-spread, weak background current and, in the model, several regions of stronger currents [Figure 3.8]. The low-period current is the only real response of the HFDRS, aside from an increase in noise. The model shows three distinct regions of stronger currents, one in the east near the KOK HFDRS site, one just west of Diamond Head Crater, and one in the west, near Barber's Point. The anomalous currents in these areas start in the west and move towards the east, in the likely direction of initial propagation. After 1.5 h, the traveling component of the radial currents at these locations is replaced by an apparent standing wave pattern of reflections back and forth across the eastern and western regions. The bend in the coastline just west of Diamond Head Crater is too small to evaluate whether it presents the same reflective pattern. There is a major drop in current strength after about 2 h, and the energetic currents are completely gone after a further 2 h for the two eastern region and 6 h for the currents near Barber's Point. All three of these regions have shallow bathymetry in the area.

Taking the average of the eastern region and the western region individually, despite the fact that said regions do not have energetic currents in the HFDRS data, shows that the two sources of data are quite different [Figure 3.9]. The eastern region average currents show only weak, low-period currents for the HFDRS and a stronger, shorter period oscillation for the model. That model oscillation has a period of 17 min. For western region currents, the match in phase and amplitude is pretty good, but that belies the true situation: the HFDRS shows only the low-period flow while the model is averaged over a traveling feature, leaving the low-period flow intact. The western region low-period flows are primarily oscillating at 43 min. EOF analysis of the near-shore area shows that the HFDRS and model data sets capture different processes in the near-shore area [Figures 3.10 and 3.11]. The HFDRS EOF maps have large features that stretch far from the coast, while those in the model are small regions that hug the coast. HFDRS EOFs up to mode 4 do not have significant errors; while NEOWAVE EOFs up to mode 5 do not have large errors, modes 2 and 3 are indistinct.

3.4 Linked Oscillations

In the modeling studies on tsunami resonance in Hawaii (Munger and Cheung 2008), the areas of spectral amplitude maximum stretch from Penguin Bank to the south shore of Oahu. This indicates that

there should be a connection between the two areas that is visible with currents. Maps of spectral amplitude across the entire area show that there are some higher spectral amplitudes near-shore at the same periods as over Penguin Bank [Figure 3.12]. The phases show that there is a smooth transition from Penguin Bank to the near-shore in the model or, as in the 43-min plots, the area from Penguin Bank to the shore has the same phase, but there is a lot of phase noise in the HFDRS over the deeper water between the two areas of interest [Figure 3.13].

Another way of looking at the linkages between near-shore oscillations and Penguin Bank is to treat the EOF time series over each area as predictors in a regression analysis. The regression coefficients (normalized to a maximum magnitude of 1) mapped over the area for each EOF time series show that the first HFDRS modes in both the near-shore and over Penguin Bank are closely linked, though the other HFDRS modes are not [Figure 3.14]. For the model, there is some expression of Penguin Bank modes in the near-shore and near-shore modes over Penguin Bank, but no two modes are as close as the HFDRS first modes are [Figure 3.15].

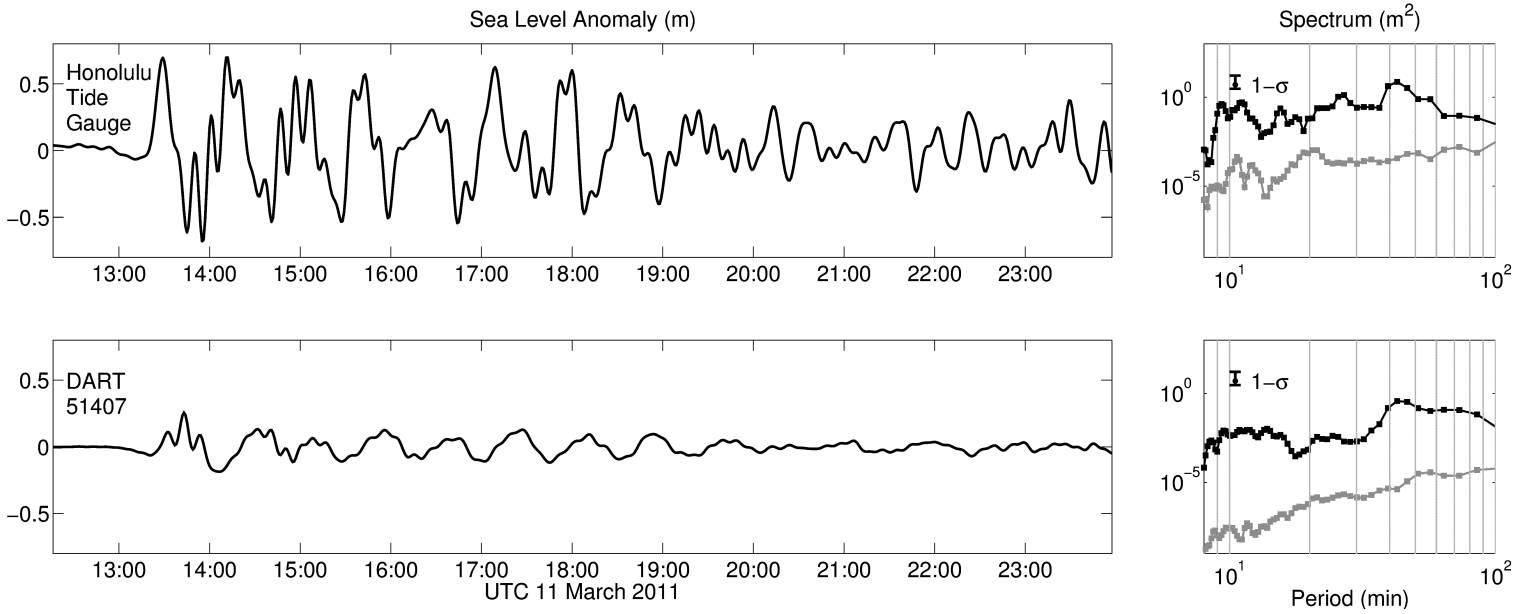

Figure 3.1. Seal level anomalies (left) and amplitude spectra $|\psi^2|$ (right) from the Honolulu tide gauge (top panels) and DART buoy 51407. The grey spectral line is from before the tsunami, while the black line is during the first 6 h of the tsunami. Every second point in the spectra is independent.

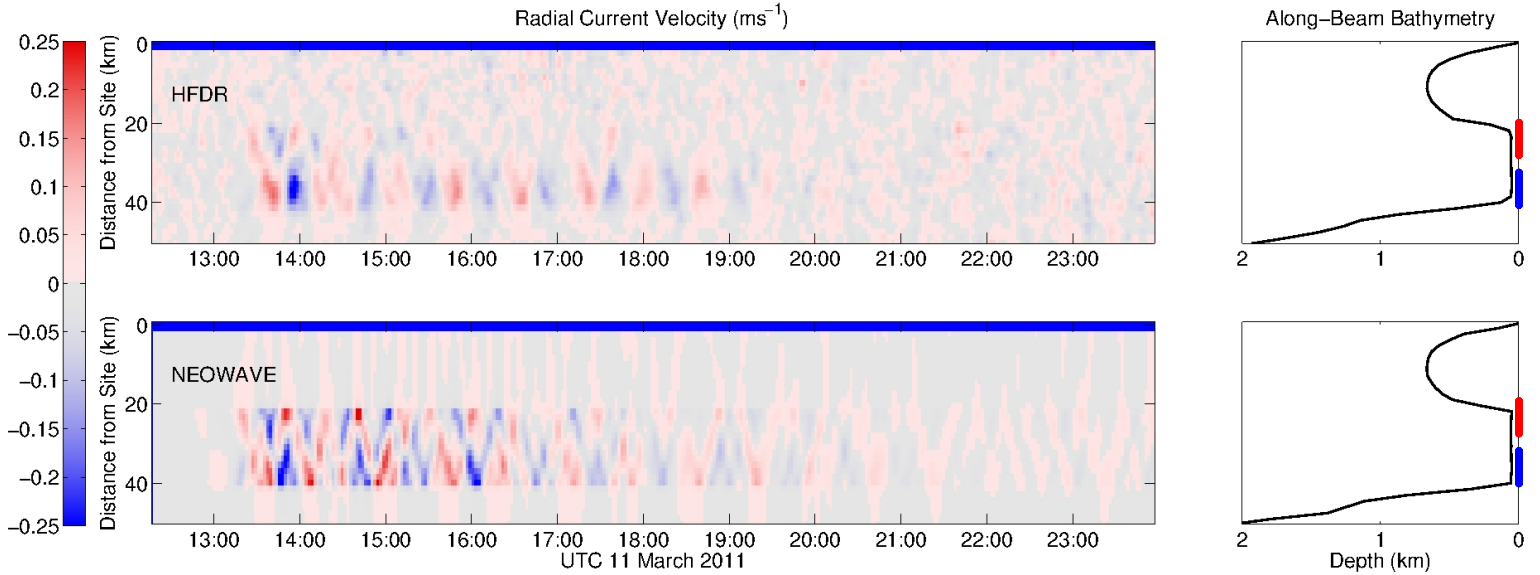

Figure 3.2. Residual radial current velocity following filtering(color) along the 161° beam angle, which crosses Penguin Bank, with the ordinate and abcissa being distance from the site and time, respectively. The KOK HFDRS data is in the top panel, and the NEOWAVE data is in the bottom panel. Along-beam bathymetry is at the right, with actual model bathymetry in the lower panel. The north Penguin Bank region is marked in the bathymetry in red, and the south Penguin Bank region is in blue.

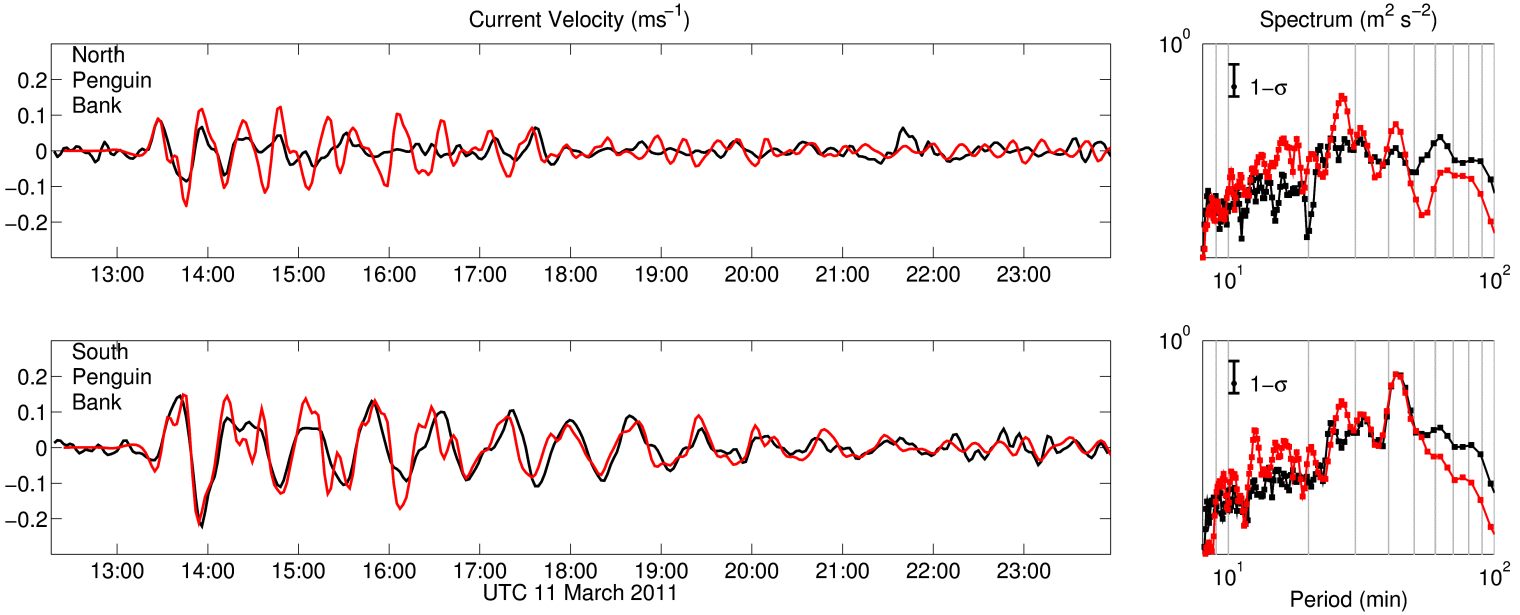

Figure 3.3. Radial velocity averaged along the 161° direction over the north bank (top) and the south bank (bottom), along with spectral amplitude $|\psi^2|$ (right). KOK HFDRS data is in black, and NEOWAVE model data is in red. Every second spectral point is independent.

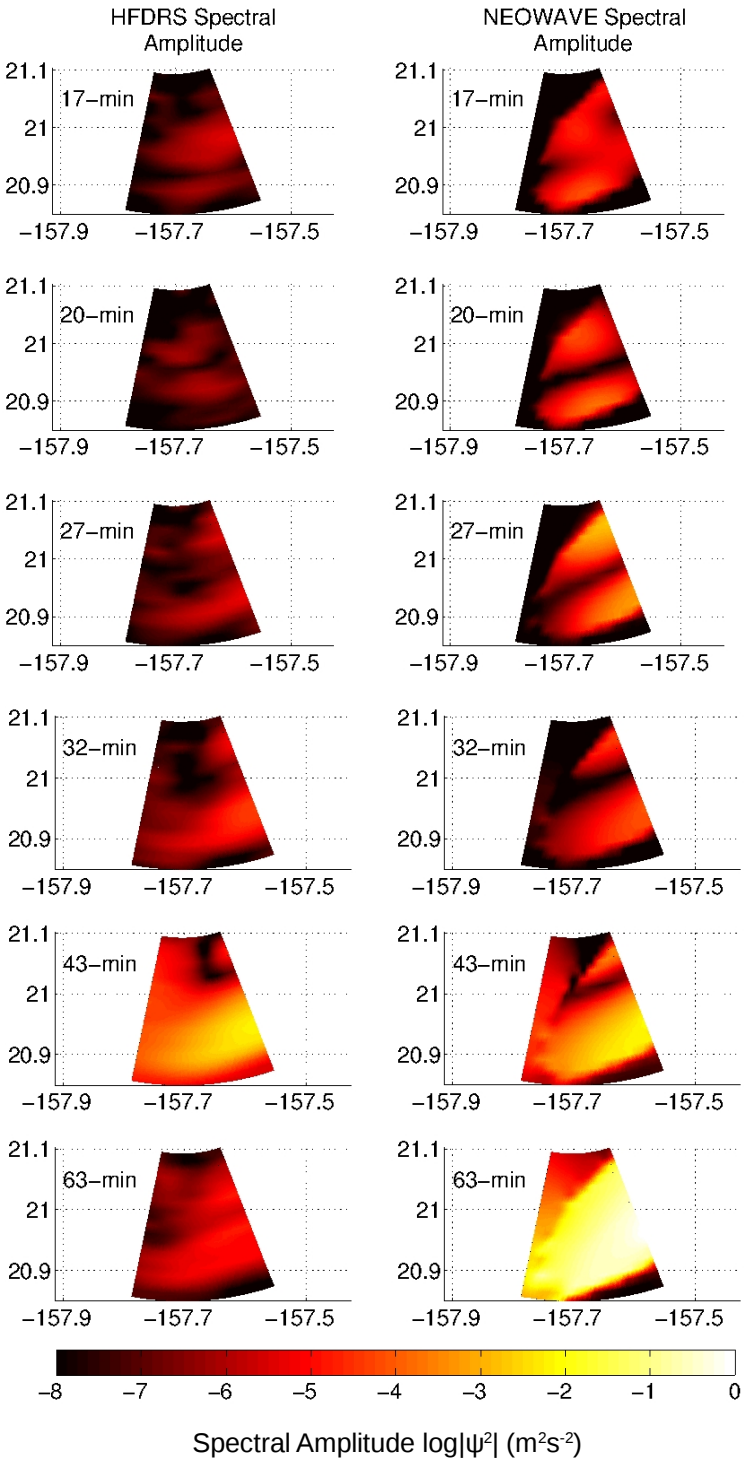

Figure 3.4. Maps of spectral amplitude $|\psi^2|$ over the Penguin Bank region at given periods, with KOK HFDRS data on the left and NEOWAVE model data on the right.

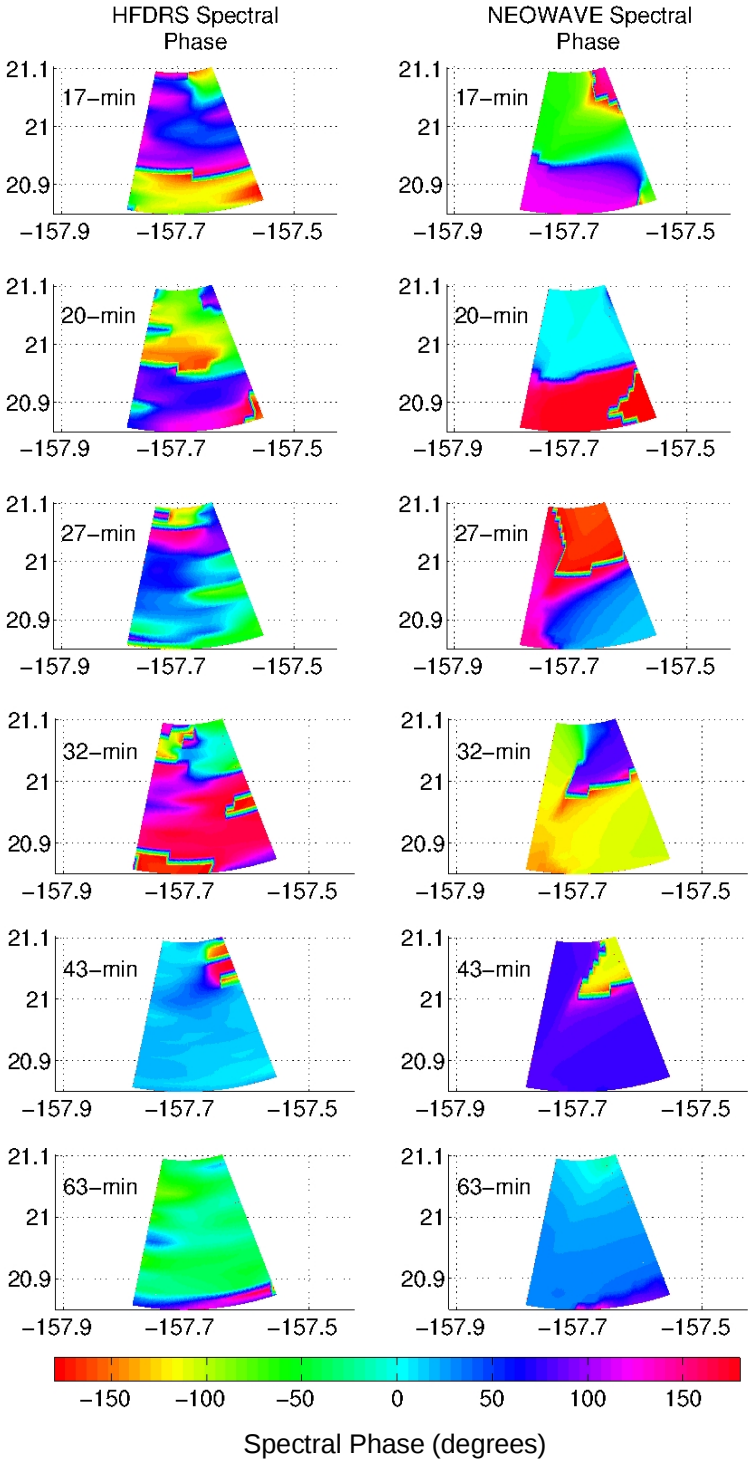

Figure 3.5. Maps of spectral phase over the Penguin Bank region at given periods, with KOK HFDRS data on the left and NEOWAVE model data on the right. Note that comparisons between HFDRS and NEOWAVE should be done through phase patterns only.

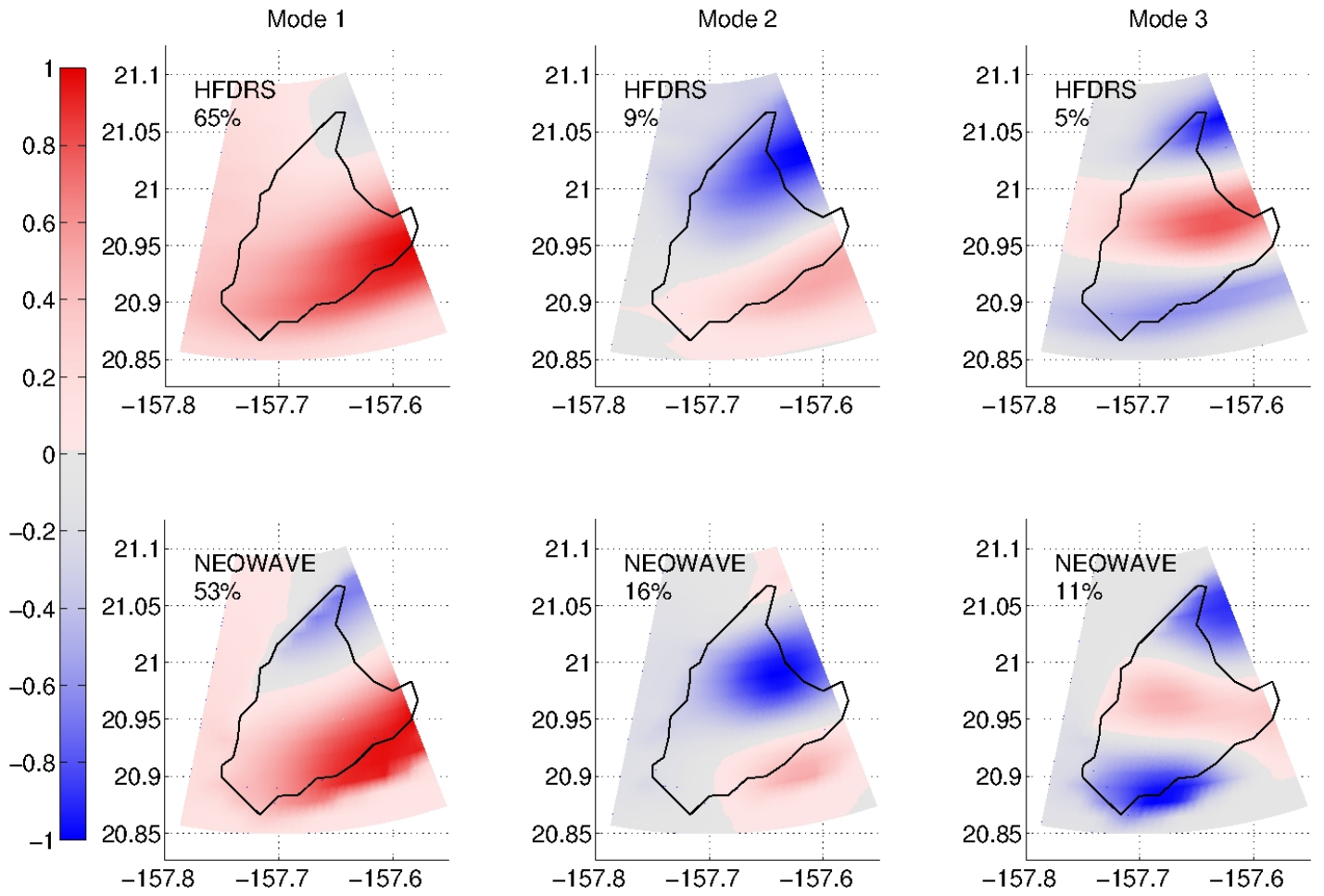

Figure 3.6. First three Empirical Orthogonal Function (EOF) maps for KOK HFDRS (top) and NEOWAVE (bottom) over the Penguin Bank region, showing percent variance explained. Note that the values have been normalized to one. The black line is the 50-m isobath showing the crest of the bank.

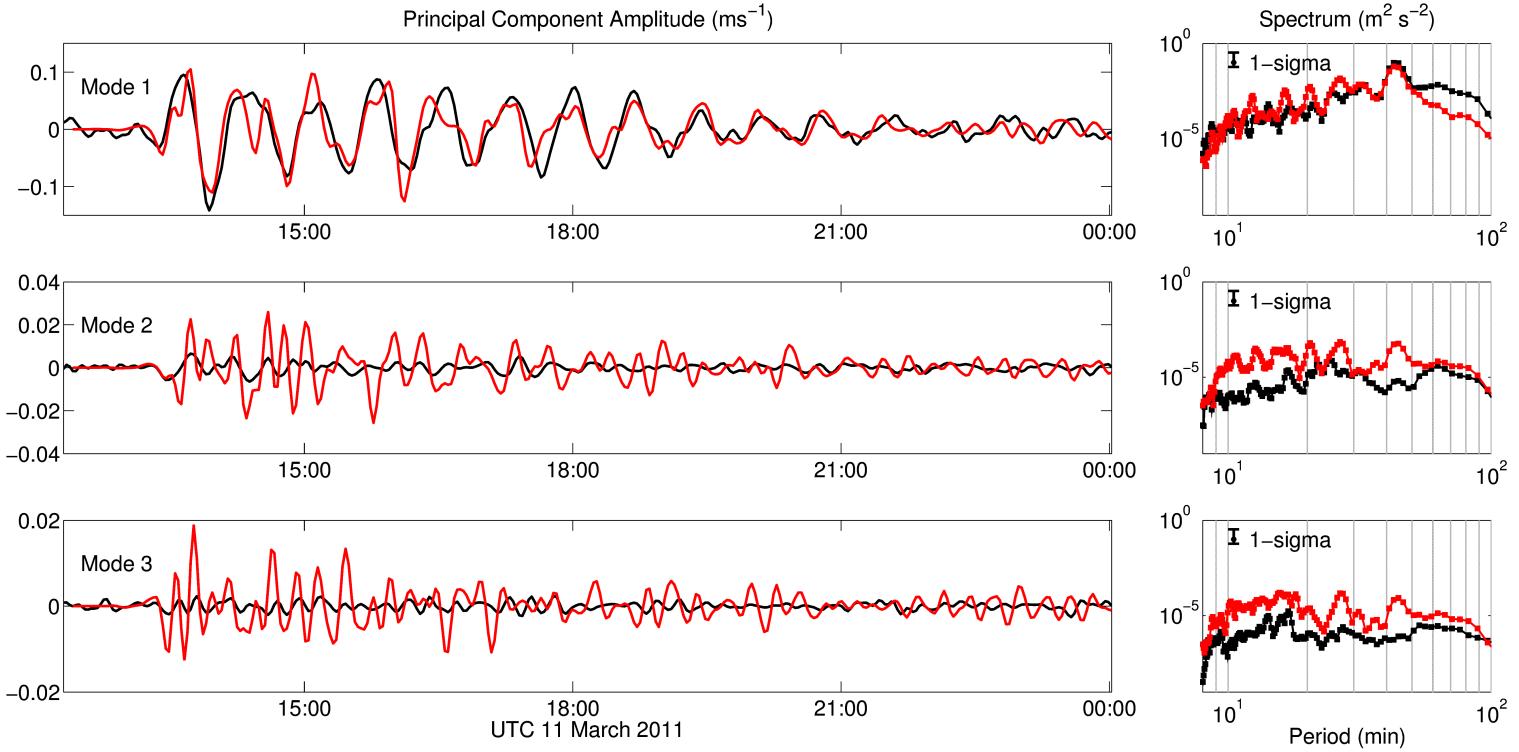

Figure 3.7. First three EOF time series of the empirical orthogonal function analysis over the Penguin Bank region. Spectral amplitudes $|\psi^2|$ of the EOF time series are at the right. KOK HFDRS data is in black, and NEOWAVE model data is in red. EOF time series amplitudes have been converted to current speeds. Every second spectral point is independent.

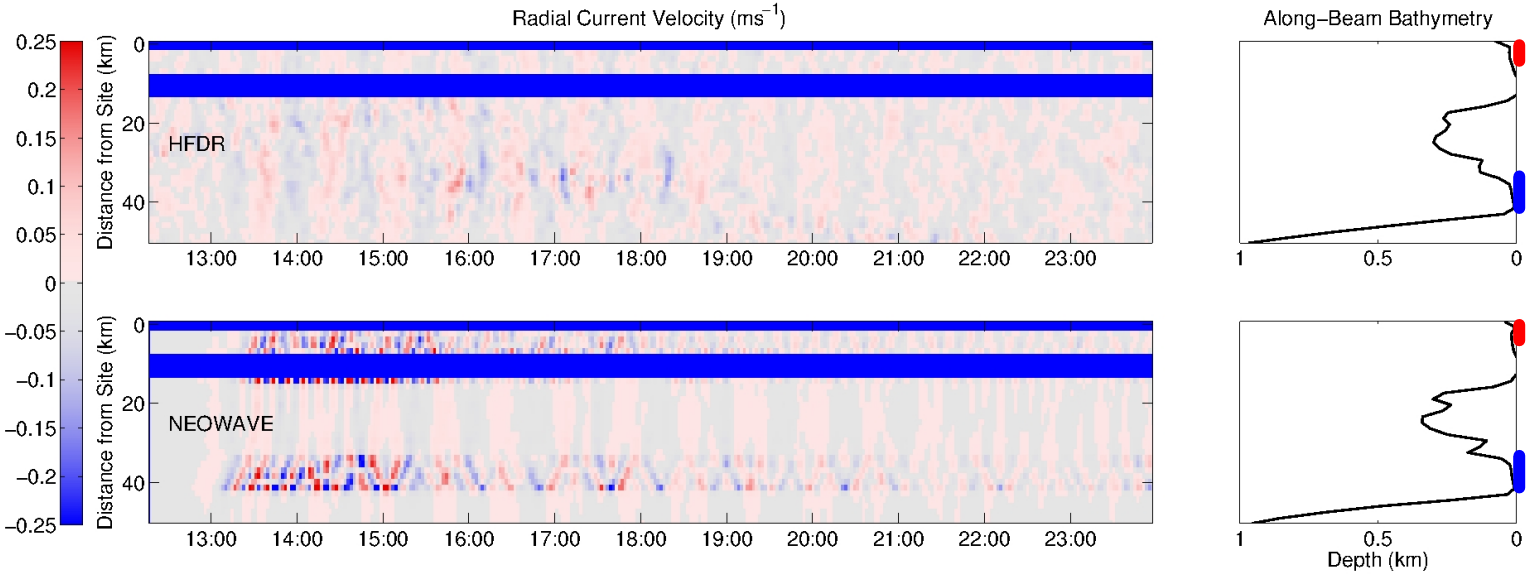

Figure 3.8. Residual radial current velocity following filtering (color) along the 274° beam angle, which lies in the near-shore region, with the ordinate and abscissa being distance from the site and time, respectively. The KOK HFDRS data is in the top panel, and the NEOWAVE data is in the bottom panel. Along-beam bathymetry is at the right, with actual model bathymetry at the bottom. The eastern region is marked in the bathymetry in red, and the western region in blue.

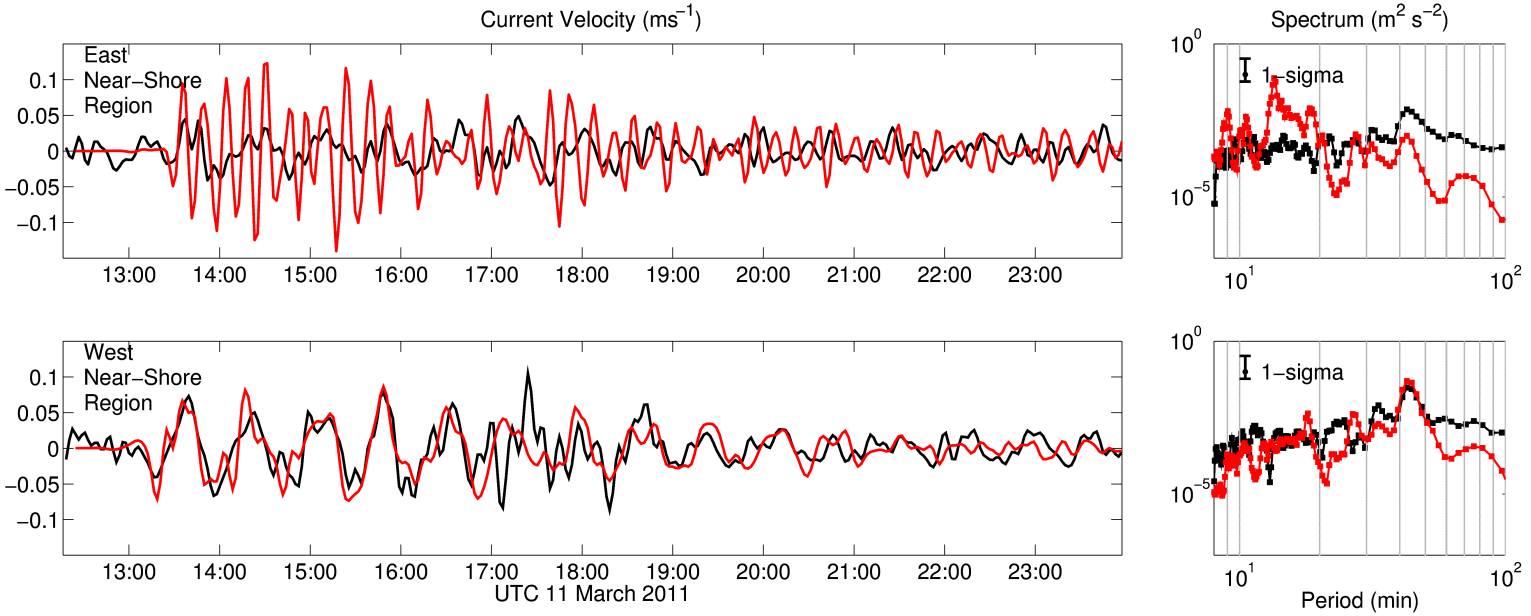

Figure 3.9. Radial velocity averaged along the 274º direction over the eastern region (top) and the western region (bottom), along with spectral amplitude $|\psi^2|$ (right). KOK HFDRS data is in black, and NEOWAVE model data is in red. Every second spectral point is independent.

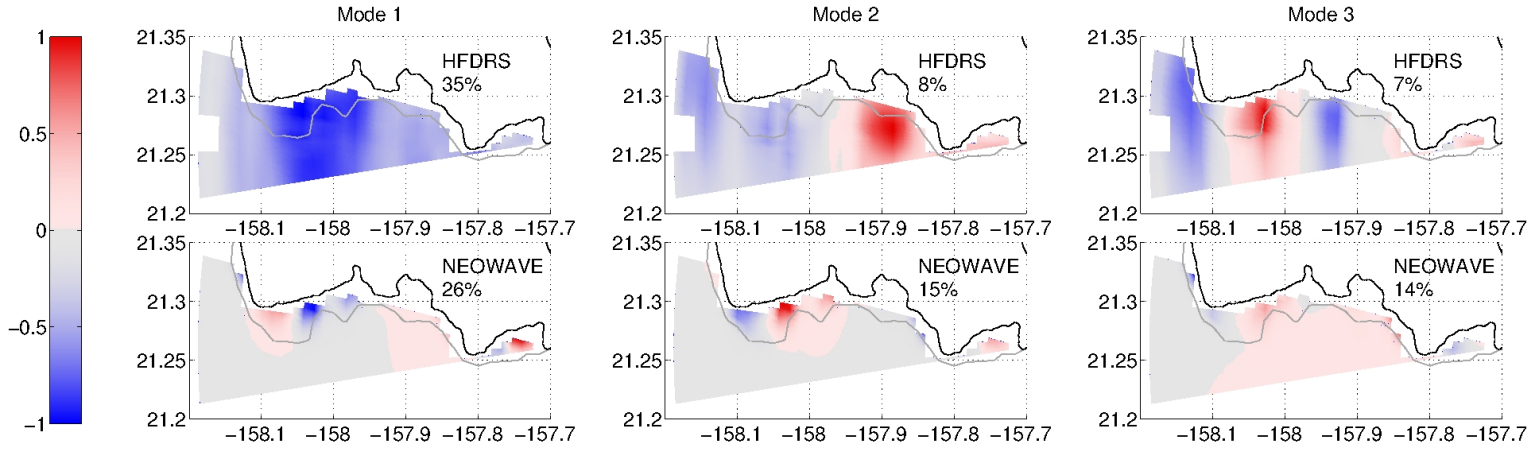

Figure 3.10. First three EOF maps for KOK HFDRS (top) and NEOWAVE (bottom) in the near-shore region, including percent variance explained. Note that the values have been normalized to one. The black line is the shore and the grey line is the 50-m isobath.

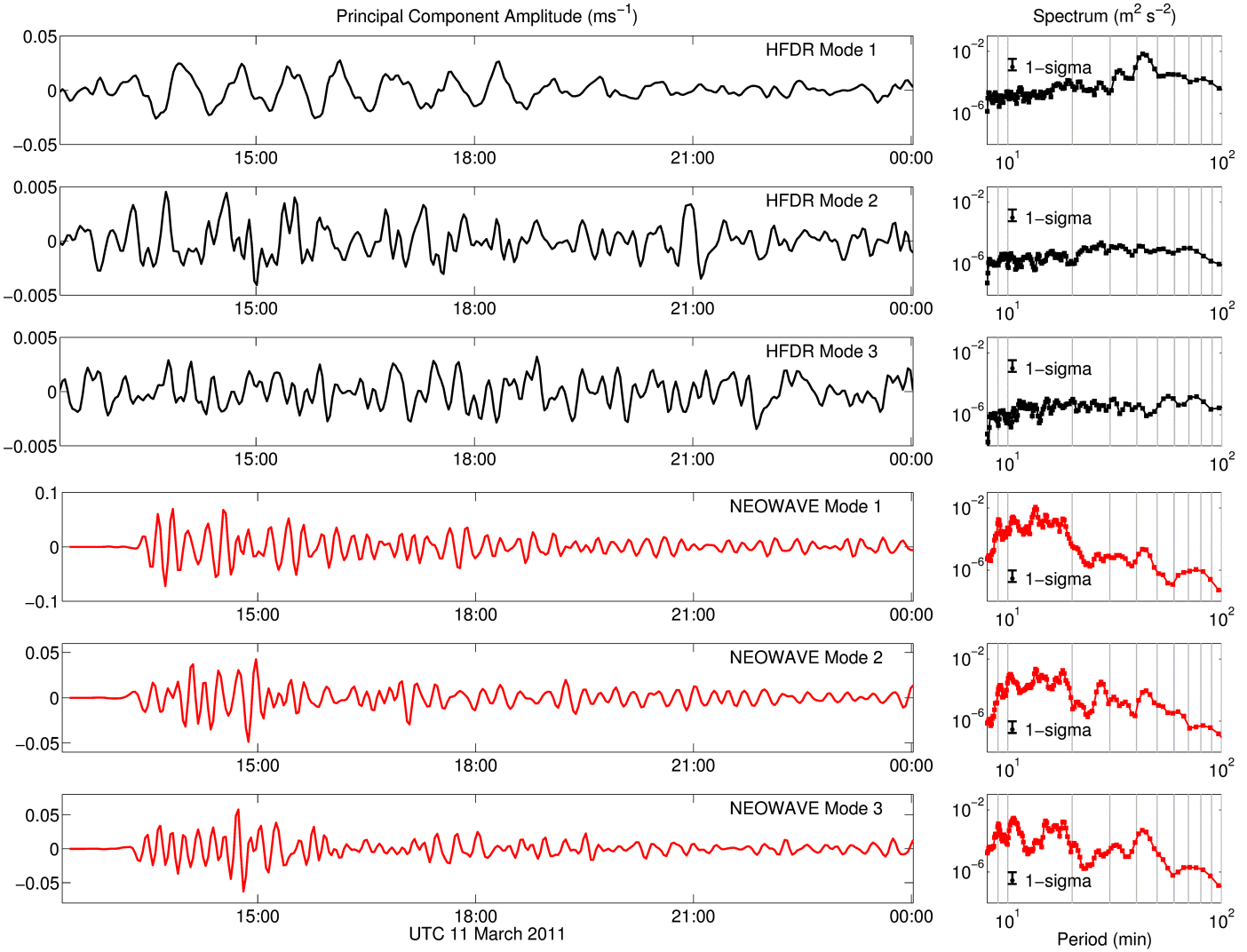

Figure 3.11. First three EOF time series of the empirical orthogonal function analysis in the near-shore region. Spectral amplitudes $|\psi^2|$ of the EOF time series are at the right. KOK HFDRS data is in black on the top, and NEOWAVE model data is in red at the bottom. Every second spectral point is independent.

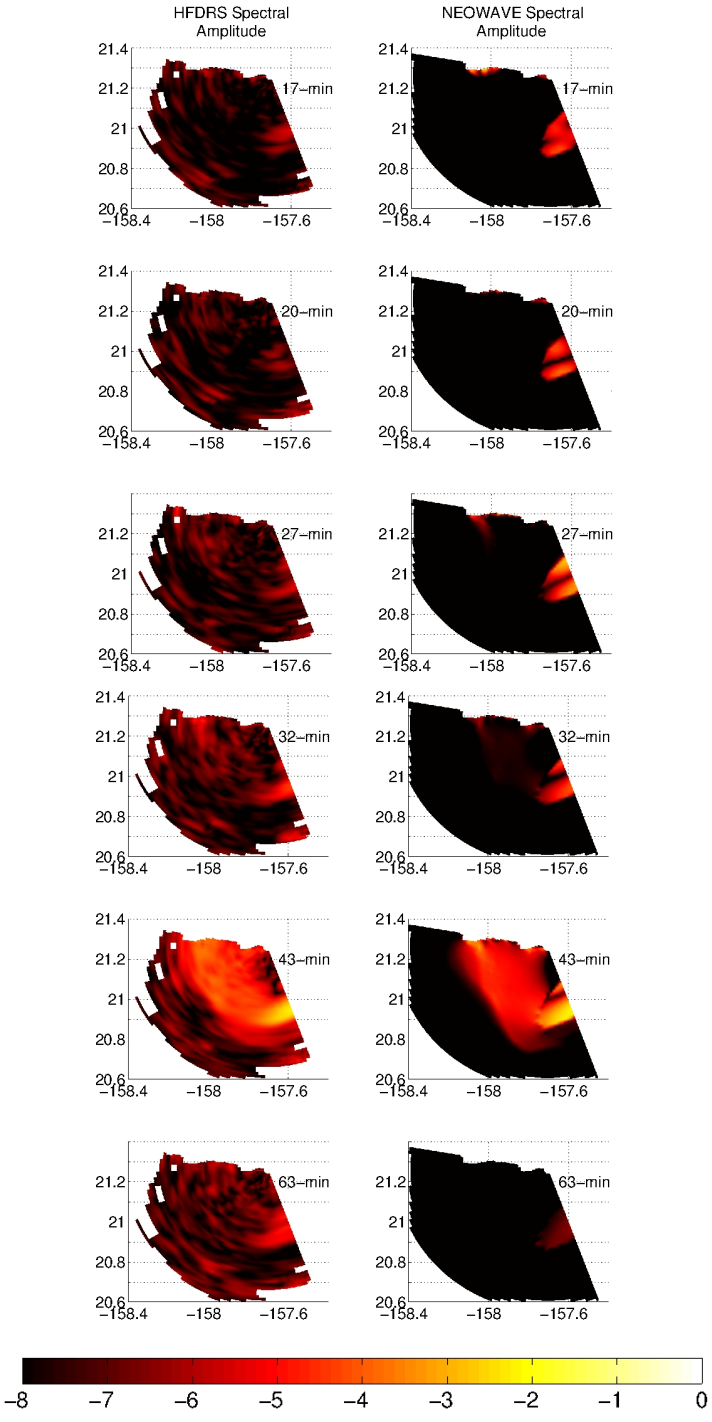

Figure 3.12. Spectral amplitudes $|\psi^2|$ for HFDRS (left) and NEOWAVE (right) at given periods over the HFDRS coverage area. .Note that the values are the log of the amplitude.

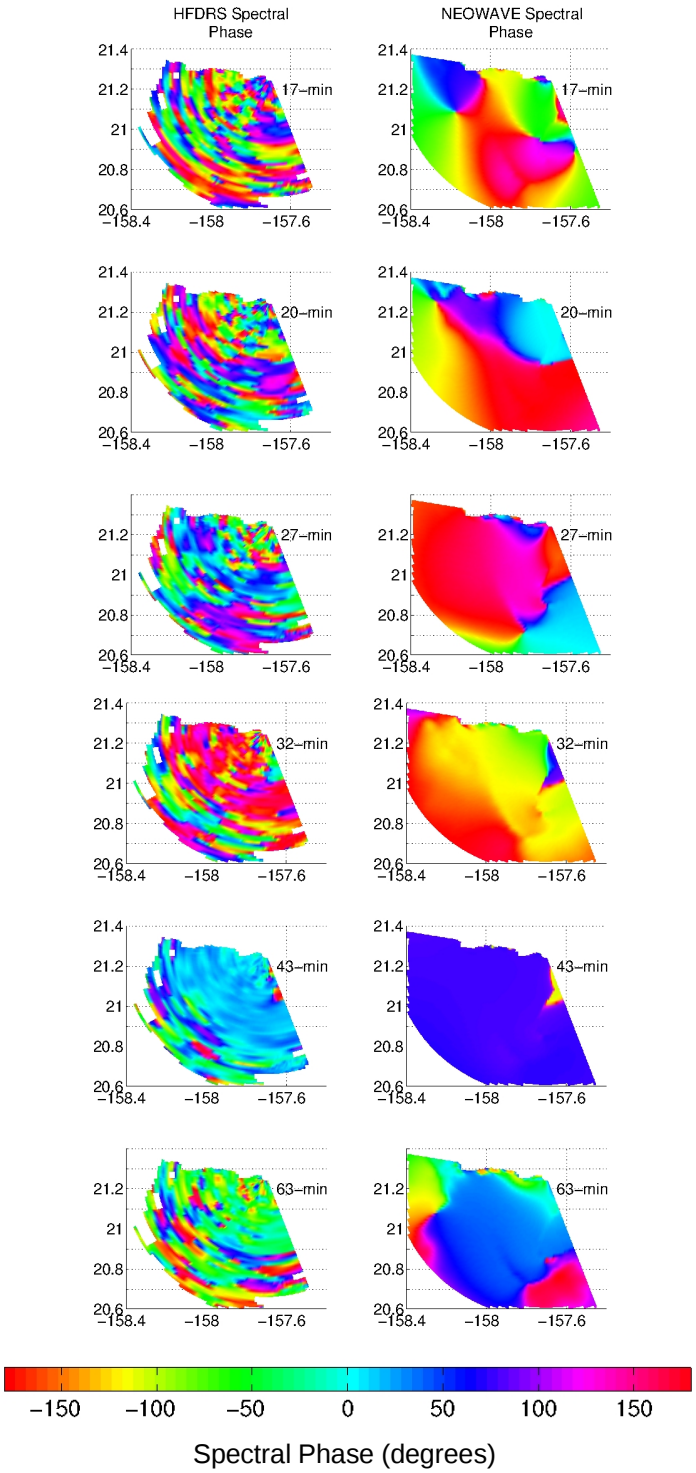

Figure 3.13. Spectral phases for HFDRS (left) and NEOWAVE (right) at given periods over the HFDRS coverage area. Note that phase angle comparisons should be done with patterns only.

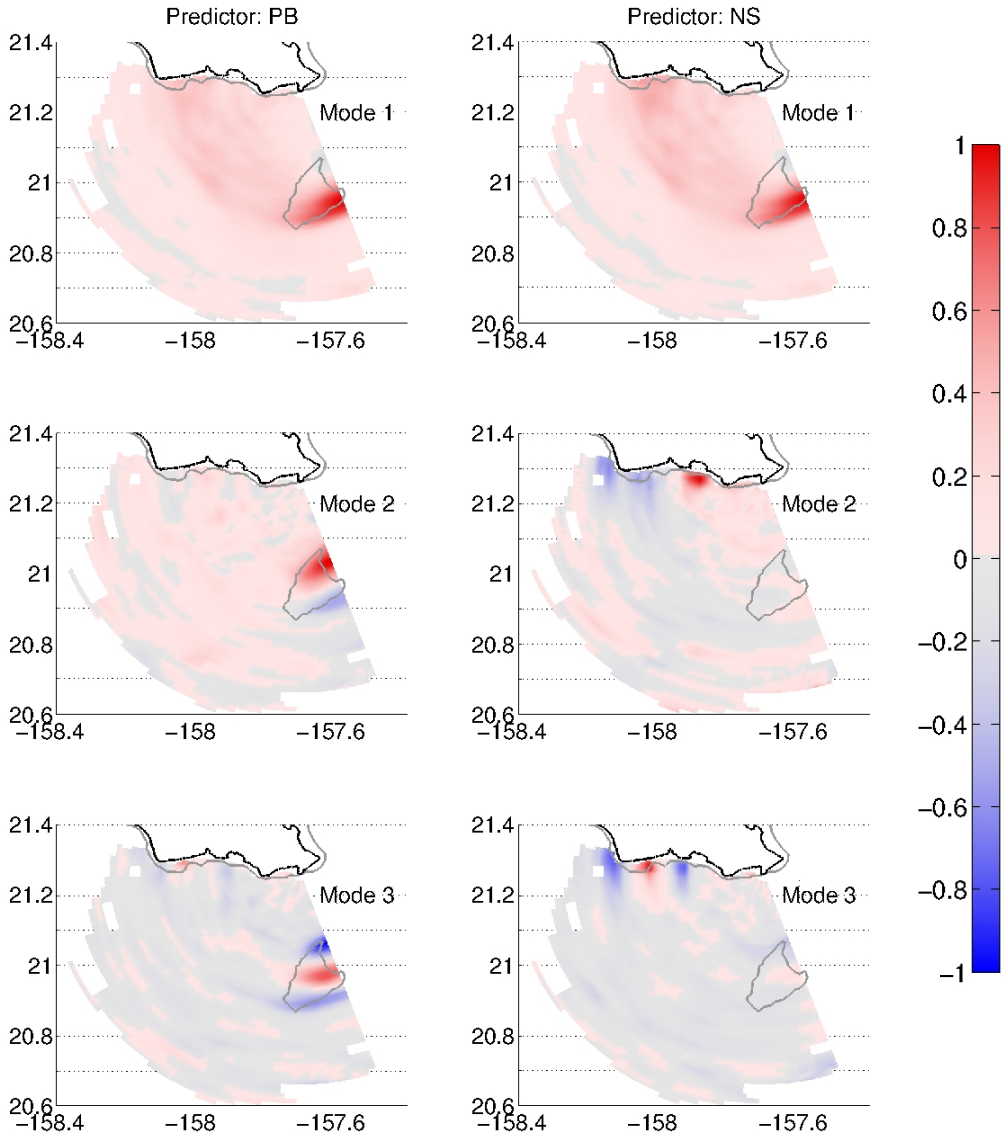

Figure 3.14. Regression coefficients for treating the HFDRS Penguin Bank region EOFs as predictors (left column) and the HFDRS near-shore region EOFs as predictors (right column). Note the strong similarities between the top two plots, and the variability in deeper waters in all plots.

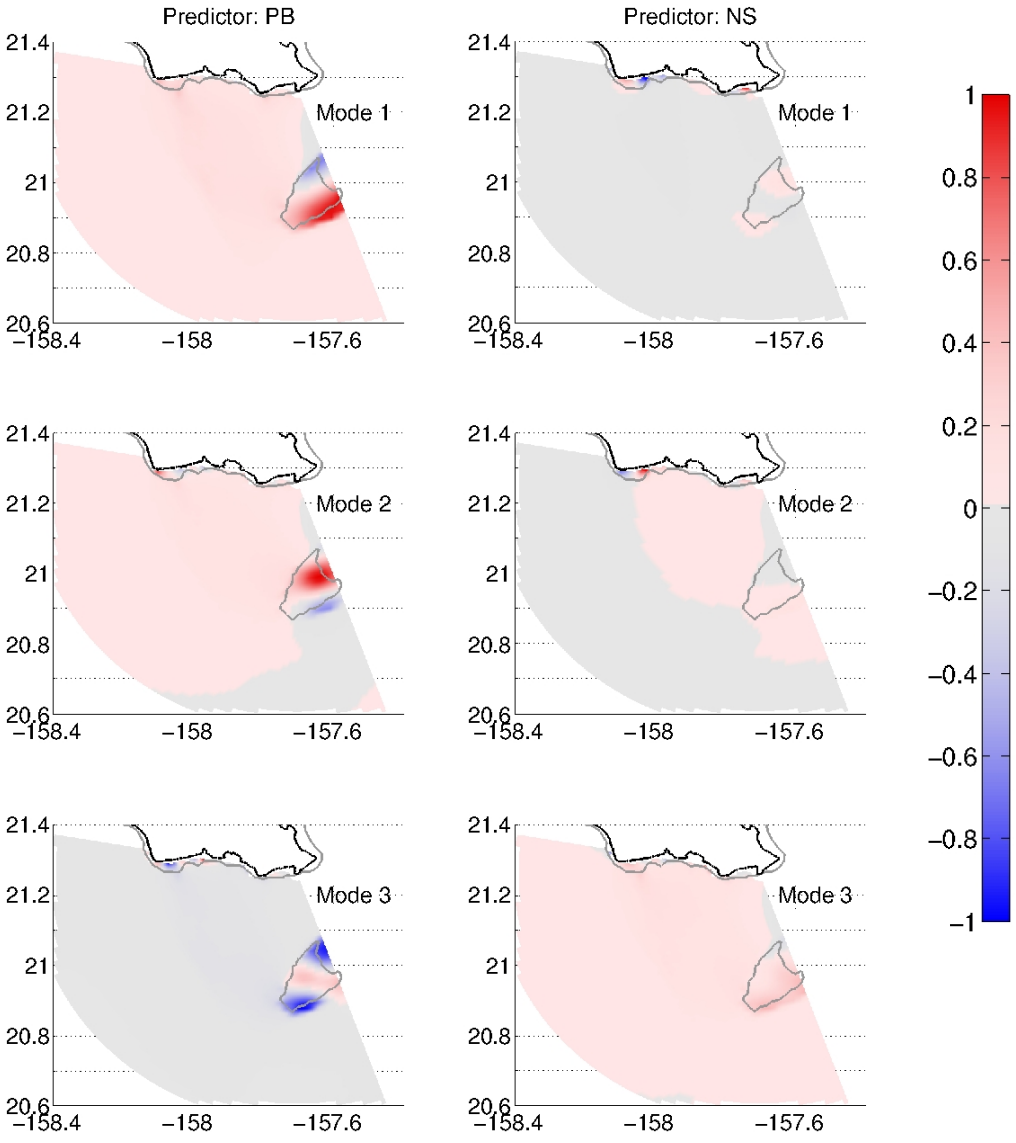

Figure 3.15. Regression coefficients for treating the NEOWAVE Penguin Bank region EOFs as predictors (left column) and the NEOWAVE near-shore region EOFs as predictors (right column). Note the weak amplitude maximum in the top left plot, and the lack of similarities between the two columns.

CHAPTER 4
DISCUSSION

4.1 Tsunami Response

Sea level measurements show the tsunami arrival in the study area as long-period waves with weaker, shorter-period components [Figure 3.1]. There is 43-min resonance both in Honolulu Harbor and across the Oahu-Hawaii Island area, with shorter-period oscillations in the harbor from harbor resonance (9–11 min) and leaking of other resonant modes (27-min) into the harbor. There is an effect from shoaling, given that the Honolulu tide gauge is in less than 10 m of water while DART 51407 is in 5700 m of water. The complex refraction and diffraction that takes place before and during the tsunami's arrival in Hawaii make it possible for the parts of the tsunami wave front that reached the Honolulu tide gauge and the DART buoy to be of different wave amplitude, shoaling effects aside. Munger and Cheung [2008] showed that there is a strong 43-min mode of oscillation that covers the entire island chain, which agrees with the response shown west of Hawaii Island in DART 51407 data and in the Honolulu tide gauge data as the mode reaches into Honolulu Harbor. As an enclosed harbor, Honolulu Harbor, where the Honolulu tide gauge is located, would have resonant modes of its own. Cheung et al. [2013] found that the resonant modes for Honolulu Harbor are 10.5 and 15 min, which are similar to the 9-11 and 16 min waves seen in the Honolulu tide gauge data. The 27-min mode around Maui Nui [Cheung et al., 2013], which is composed of the islands of Molokai, Lanai, Maui, and Kahoolawe and their shared shelves, may also leak into Honolulu Harbor judging by the 27-min spectral peak in the Honolulu tide gauge data.

The strong response over Penguin Bank in the radial surface currents was also characterized by long-period oscillations, with differences in strength and current duration existing between the northern and southern parts of the bank [Figure 3.2]. These differences are present at nearly all periods and are the most significant characteristic of the tsunami-induced flow over Penguin Bank. Inferring general information about sea level changes over the bank for the radial surface currents, the three most significant motions, as gleaned from EOF analysis, are two standing half waves and one standing full wave centered over Penguin Bank [Figure 3.6]. The first two modes show water entering and leaving Penguin from both sides, which is a standing half wave in sea level, with nodes on the bank edges and an anti-node in the center. The third mode shows currents moving water from one part of the bank to another (north to south, and vice versa), which is a standing full wave in sea level, with nodes on the edges and in the center and anti-nodes about 1/3 and 2/3 of the way from the northern edge of the bank. These modes match up with some of the sea level modes in Figure 4.1, which shows several different standing half and

full waves over Penguin Bank.

The near-shore 43-min response is weaker and stretches along the south shore from the HFDRS site to Barber's Point [Figure 3.8]. The model shows strong evidence for the existence of edge waves in the establishment of the back and forth standing wave pattern of reflections [Bricker et al., 2007], but the HFDRS does not. EOF analysis revealed the vast differences in the structure of the near-shore radial currents seen in the HFDRS and model [Figure 3.10]. Though there are weak similarities between some of the EOF maps (HFDRS and NEOWAVE modes 1; also HFDRS mode 3 and NEOWAVE mode 2), the angular smearing of the areas of maximum amplitude due to decreased angular resolution at high steering angles [Appendix B.3] makes any comparison suspect, not to mention the vast differences in the EOF time series and their spectra for those modes [Figure 3.11]. Additionally, the strong possibility of azimuthal side lobe contamination, or mapping of currents into an angle other than where they occur because of side lobes [Appendix B.3], of the near-shore HFDRS currents means similarities found in a comparison of it with model data will not pass scrutiny.

The exact regions in Penguin Bank and the near-shore that are a part of the same oscillatory mode are difficult to determine in the HFDRS data because of decreased angular resolution at high steering angles. Both Penguin Bank and the near-shore region are at the edges of the coverage area for the KOK HFDRS, which is where the angular resolution of the instrument is the worst. This decrease in resolution can be easily seen in the HFDRS spectral amplitude maps [Figure 3.12] and regression coefficient maps Figure [3.14] where the areas of maximum amplitude in both regions are curved precisely along angular arcs and also appears smeared. The extension of the 43-min Penguin Bank spectral amplitude maximum towards the near-shore region in a near-perfect arc may be indicative of azimuthal side lobe contamination[Figure 3.12].

4.2 Two-Dimensional Model Validation

There has been no two-dimensional validation of tsunami modeled currents before. Point validation is usually fairly sparse; note that 1 DART buoy, 5 tide gauges, 1 pressure sensor, and 18 ADCPs were used to validate NEOWAVE for the whole area surrounding the main Hawaiian Islands, an area greater than 67,500 km^2. Two-dimensional validation near the coast would give more confidence in a model's measurements of near-shore currents which play important roles in the evolution of the run-up and inundation, the two parts of a tsunami that cause the most damage to humans and property. HFDRS maps surface currents over an area, which could be used to validate tsunami models.

The KOK HFDRS and NEOWAVE showed great similarities in the currents within the KOK

coverage area. The strong response that occurred primarily over Penguin Bank shows numerous similarities. The currents on the north bank match up quite well for the first hour, but then the comparison is no longer good [Figure 3.2]. On the south bank, the model and HFDRS currents match well in terms of both amplitude and phase, for the duration of the strong response. The spectra show a good match for the 43-min peak. The spectral modes show good agreement as well, and the phase changes of these modes are close over Penguin Bank [Figures 3.4 and 3.5]. The EOF maps are quite similar, though only the first EOF time series shows a good agreement between model and HFDRS [Figures 3.6 and 3.7].

Plotting the NEOWAVE data versus the KOK HFDRS data for various regions [Figure 4.2] allows for an analysis of the linearity of the relationship between the two data sets. Even slight variations in the orientation of the data in multi-dimensional space may result in different EOFs for similar data sets, but the similarities noted earlier between the HFDRS and model EOF maps [Figure 3.6] encourage such a comparison despite these potential differences. The relationships for the south bank, EOF map 1, and EOF time series 1 are linear, which is expected given the good comparison between NEOWAVE and HFDRS data for those locations found earlier. The plots for the north bank, EOF time series 2, and EOF time series 3 are well-scattered, indicating a poor linear relationship and a bad match between model and HFDRS data. For EOF maps 2 and 3, the plots show a fairly linear segment with several extensions of points that curve back towards the origin, which is indicative of several different relationships, not all linear, within the same comparison. Interestingly, these extensions are found in areas of the Penguin Bank region where there is angular smearing due to decreased angular resolution of the HFDRS, so they may in fact be artifacts.

4.2 Problems Associated with HFDRS

The HFDRS data is not without fault, and expecting the model to exactly reproduce every facet of the data would not be a reasonable goal [Appendix B]. The KOK HFDRS shows clear signs of decreased angular resolution at large steering angles in the form of angular smearing of currents in both areas of potential interest [Figure 3.14]. Both Penguin Bank and the near-shore area are at the edges of the coverage area, so the KOK HFDRS is not ideally positioned to monitor these areas. Also, the relatively strong expression of tsunami-related modes in fairly deep waters between Penguin Bank and the near-shore suggest azimuthal side lobe contamination. The inverse relation between temporal resolution and velocity resolution can also cause problems, particularly with a weak tsunami in an area with high-frequency resonant oscillations. Care must be taken in using HFDRS data for model validation because a model that reproduces these errors would be wrong, despite matching the data more closely.

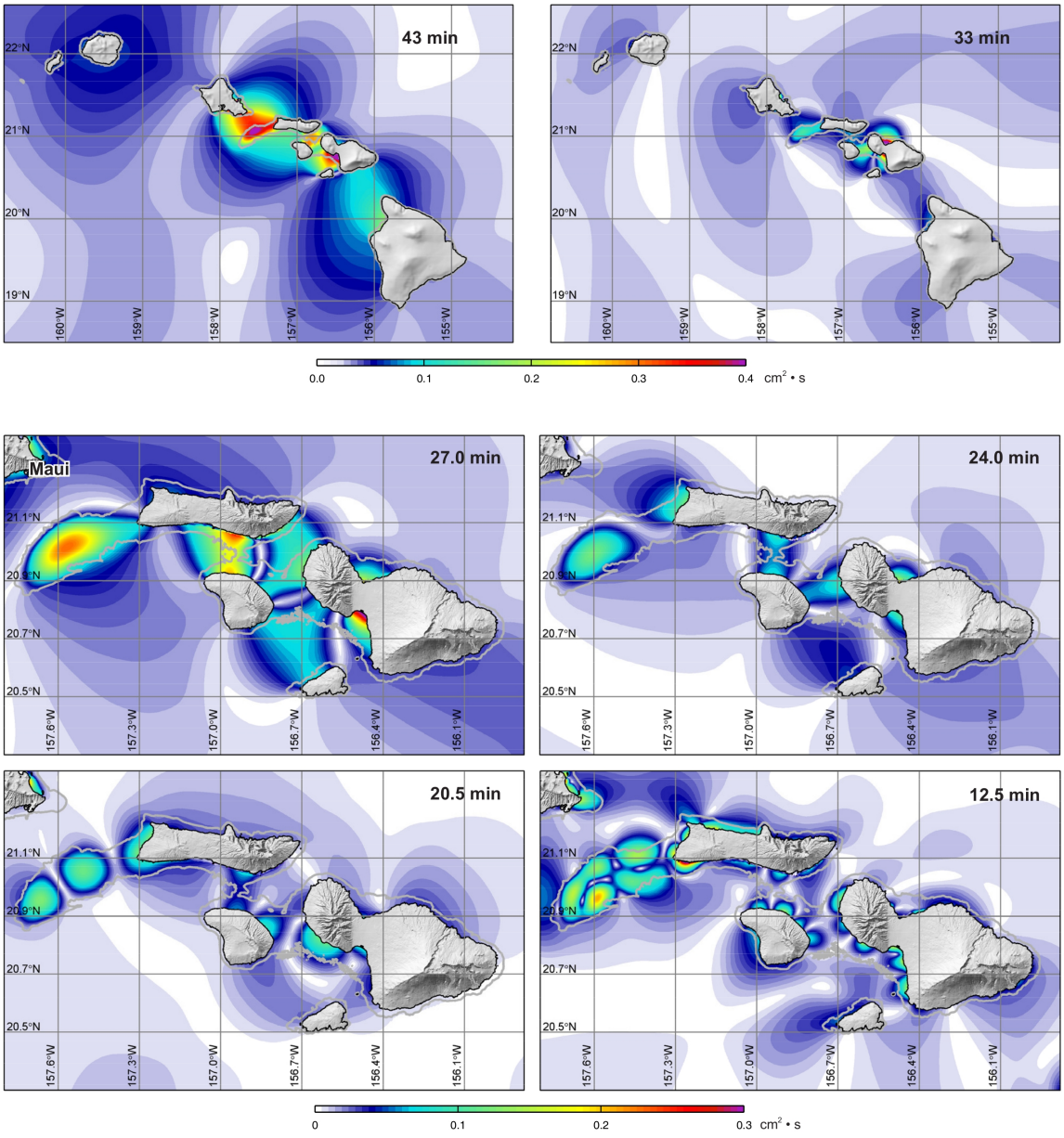

Figure 4.1. Spectral amplitudes of anomalous sea level from NEOWAVE at different periods around the Hawaiian Islands (upper) and Maui Nui (lower). From Cheung et al. [2013], Figures 5 and 9.

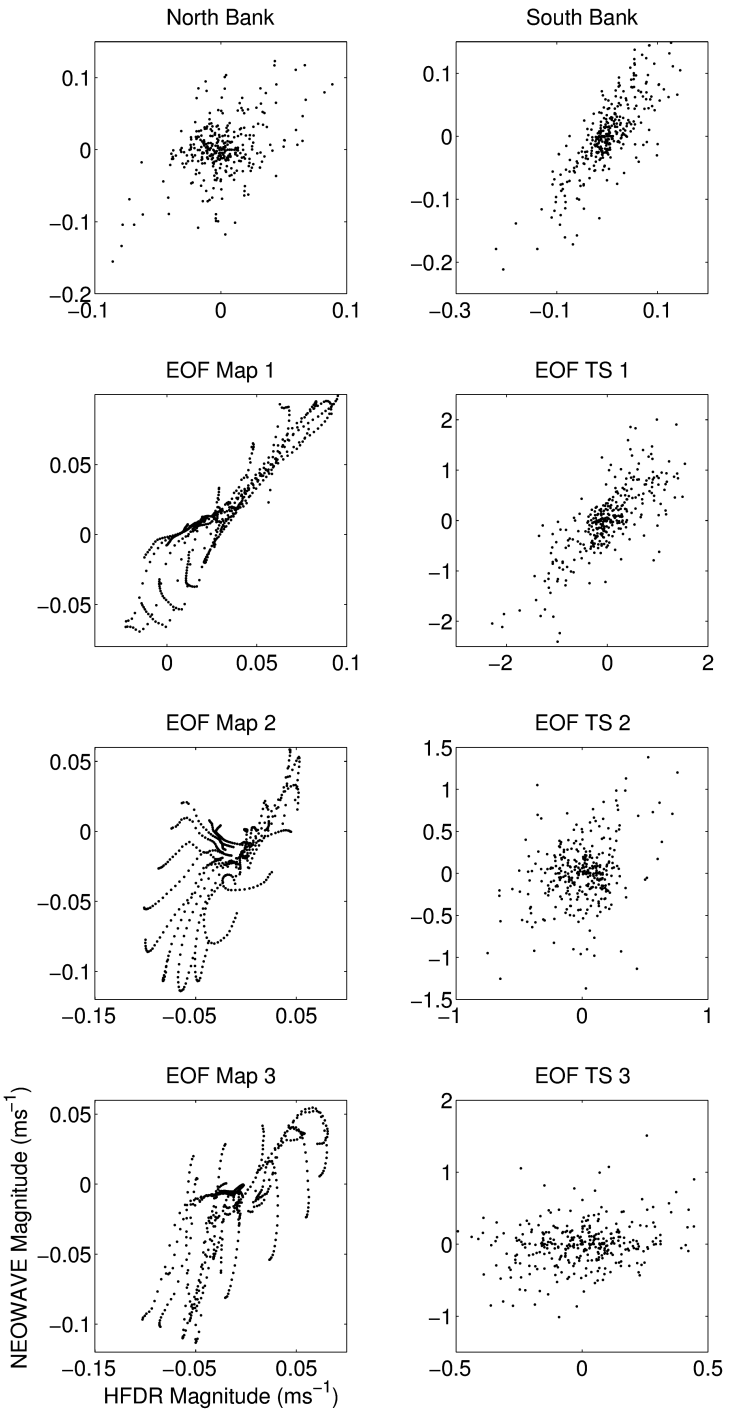

Figure 4.2. Scatter plots of NEOWAVE data versus KOK HFDRS data for north bank, south bank, EOF map 1, EOF time series (TS) 1, EOF map 2, EOF TS 2, EOF map 3, and EOF TS 3. The most linear of these relationships are found on south bank, EOF map 1, and EOF TS 1.

CHAPTER 5
CONCLUSION

The KOK HFDRS detected the resonant response of the 2011 Tohoku tsunami south of Oahu. The currents over Penguin Bank indicate a suite of standing waves form over the bank, some of which coincide with the 43-min oscillations in the near-shore HFDRS data, the Honolulu tide gauge data, and DART 51407 data supporting the idea that Penguin Bank is a probe for resonance around the Hawaiian Islands. Strong currents, or the strongest component of a current, match well between HFDRS measurement and tsunami model over Penguin Bank. The major modes, both in terms of spectral density and EOF analysis, show good spatial agreement over Penguin Bank. In the near-shore region, a long-period, widespread oscillation was seen in both HFDRS and model, but evidence for edge waves seen in the model is lacking in the HFDRS, likely due to spatial smearing at large steering angles in the near-shore region. Disagreements between HFDRS and the model can be categorized as spatial errors that are likely due to decreased angular resolution at high beam steering angles or azimuthal side lobe contamination, or they can be categorized as current magnitude errors that are found when current magnitudes are too low.

The use of an ideally situated HFDRS, as in one where the shallow areas of interest are fairly close in range as well as close to normal in angle to the receive array, in a similar study would be of immense interest as it would give an idea of the best-case scenario in terms of the potential contributions to model validation that HFDRS can make. This study deals with a non-ideal case, which makes clear the limitations based on such non-idealities but gives no idea of the possible true potential of the technique. Arranging two HFDRS to look at Penguin Bank at right angles to one another would also yield important results because the measurement of surface currents in two perpendicular directions would allow the reconstruction of vector currents. The full current field over Penguin Bank could then be compared with the model results, allowing for a more thorough assessment of model performance.

Tsunami warning systems may benefit from the addition of HFDRS data to the current suite of tools under certain circumstances: there is a shallow region between the generating earthquake's epicenter and a populated area that can be covered by HFDRS; the HFDRS data is processed and utilized quickly enough to be of use either before the first wave or to help in determining the drop off of tsunami energy in a local system; the warning system does not rely too heavily on HFDRS in the event that wave refraction and/or diffraction causes a maximum in tsunami strength through constructive interference that misses the shallow area of interest but not a populated area.

APPENDIX A
TSUNAMIS

A.1 Definition

Tsunamis are shallow water waves with very long wavelength and period. Even at full-ocean depth, they are accurately described by the shallow water Equations. Tsunamis are generated by any process that quickly displaces a large volume of water vertically, such as earthquakes, landslides, ice calving, meteor strikes, or strong atmospheric pressure disturbances. Because of the unpredictability of the generation events, tsunamis cannot be predicted before their generation. This makes deployment of instruments to study tsunamis problematic, especially since near-field tsunamis can reach land in min, and far-field tsunami reach across the Pacific Basin in less than one day. Extremely rapid deployment of instruments is necessary, but not always feasible.

Tsunami warning systems are based on a combination of swiftly run models based on seismic or other activity and DART (Deep-ocean Assessment and Reporting of Tsunamis) buoys, which are bottom-mounted pressure systems that can detect that cm-to-m high deep-water tsunami wave amplitudes. The models produce initial estimates that are revised based on wave amplitudes measured at DART buoys and tide gauges. Great care must be taken when issuing warnings as false alarms may cause the public to ignore future warnings.

DART buoys detect the very small wave amplitudes in deep water, but, as a tsunami propagates to shallower water, the wave height increases because the energy leaving one depth enters another depth.

$$U = \rho g z \tag{A.1}$$

is the potential energy, where U is the potential energy, ρ is the water density, g is the gravitational acceleration, and z is the height. Averaged over a single wavelength l in the horizontal *x*-direction for all water particles within the wave, which fluctuates with water level η,

$$U = \frac{\rho g}{l}\int_0^l \int_0^\eta z\, dz\, dx = \frac{\rho g}{l}\int_0^l \frac{\eta^2}{2} dx \tag{A.2}.$$

If the water level is described by $\eta = H \sin\left(\frac{2\pi x}{l}\right)$ for wave height H, then the potential energy becomes

$$U = \frac{\rho g H^2}{2l}\int_0^l \sin^2\left(\frac{2\pi x}{l}\right) dx \tag{A.3}.$$

Integration yields the final answer

$$U = \frac{\rho g H^2}{2l} \times \frac{l}{2} = \frac{\rho g H^2}{4} \quad \text{(A.4)},$$

and the equipartition of energy in a wave between kinetic energy and potential energy allows the calculation of the total energy, E, per wavelength:

$$E = \frac{\rho g H^2}{2} \quad \text{(A.5)}.$$

Flux of energy F_E within a wave is conserved,

$$F_E = E v \quad \text{(A.6)},$$

where v is the speed at which the energy travels from deep to shallow water (points 1 and 2), so that:

$$\frac{\rho g H_1^2}{2} v_{g1} = \frac{\rho g H_2^2}{2} v_{g2} \quad \text{(A.7)}.$$

Here, v_g is the group speed of the wave. This simplifies to

$$\frac{H_1^2}{H_2^2} = \frac{v_{g2}}{v_{g1}} \quad \text{(A.8)}.$$

The group and phase speeds of shallow water waves are equal, $v_g = v_p = \sqrt{gh}$, so Equation (A.8) can be written as a relationship between wave height and water depth h:

$$H_1 = H_2 \left(\frac{h_2}{h_1} \right)^{1/4} \quad \text{(A.9)}.$$

This process is known as shoaling, and arises because, as the front of the wave reaches shallow water and slows, the back of the wave continues. Water is compressed between the two ends, resulting in an increase in wave amplitude.

One consequence of shoaling is an increase in tsunami current speed. As a wave shoals, the wavelength decreases but the period remains the same. Combined with the increased wave height, the velocity of the individual water particles within wave orbits increases. This can be demonstrated considering conservation of energy density working from the kinetic energy within wave orbits ($K_E = mv^2/2$ in general, $K_E = \rho h l u^2/2$ here, for kinetic energy per wavelength K_E and water particle velocity u) for a shoaling wave:

$$\rho h_1 l_1 u_1^2/2 = \rho h_2 l_2 u_2^2/2 \quad \text{(A.10)},$$

Knowing that $v_p = l/p$, where p is the period, combined the definition of phase speed and

substituting into Equation (A.10)

$$h_1^{3/2} p_1 u_1^2 = h_2^{3/2} p_2 u_2^2 \qquad \text{(A.11)}.$$

The period of a shallow water wave does not change with shoaling $(p_1 = p_2)$, so Equation (A.11) simplifies to

$$\frac{u_1}{u_2} = \left(\frac{h_2}{h_1}\right)^{3/4} \qquad \text{(A.12)}$$

Because the wavelength of even a shoaled tsunami is so long the water particle velocity acts over a large spatial extent as a surface current. From a surface current perspective, a tsunami is a feature with bands of current that have a sinusoidal amplitude and direction at one place that repeats every tsunami-wavelength.

A.2 Traveling Waves

Tsunamis are principally traveling-wave features. Because of refraction due to bathymetric-dependent phase and group speeds, they are usually long-period wave fronts propagating perpendicular to large-scale mean isobaths. This refraction also wraps tsunami waves around features such as islands, which can create very large wave amplitudes on the shadowed side of islands where the two wrapping waves meet [Yamazaki et al., 2009]. Bathymetry can also focus tsunami energy into a beam, as the Mendocino Escarpment causes tsunami energy to focus at Crescent City, California [Kowalik et al., 2008].

Tsunamis are also subject to diffraction, or re-emission of circular wave fronts from, for example, between islands in an archipelago. Diffraction creates new, independent wave fronts that are free to interact constructively, destructively, or non-linearly, with both the original front as well as any other new fronts. Together with refraction, diffraction serves to create complex wave fronts, such that the arrival of a tsunami may be accompanied by waves much larger or smaller than the initial wave front [Song et al., 2012].

A.3 Standing Waves

The traveling tsunami waves are not the only danger. Frequently, tsunami energy is trapped in harbors, enclosed areas, or around islands and along coastlines, leading to resonant oscillations and patterns of standing waves. Because resonance is strong and may last for hours or days, it may overwhelm any tsunami signal and can be more dangerous and damaging than the actual tsunami waves.

Resonance modes are based on the characteristics of the location, as resonance in a square harbor depends on the dimensions of the harbor, for example. Tsunami waves inject energy into resonant modes, which have low losses and may continue to oscillate for days. Tsunamis may have one period with the

most energy, but typically there are other periods excited due to refraction, diffraction, interference, and energy smearing. Also, one resonant mode may leak energy into other modes, exciting a whole suite of oscillatory patterns.

Because resonant modes are standing waves, there is no simple relationship between water velocity and sea level anomaly as exists for traveling waves. A standing wave is made of two traveling waves moving in opposite directions, and they produce a standing wave with the same wavelength. Theoretically, if a standing wave is completely symmetric and both of its component traveling waves are identical except for the direction of propagation, one-half of the maximum velocity on each node is the maximum water particle velocity of each component traveling wave at its crest. From that, the maximum height of each component traveling wave can be calculated. That would then be one-half the maximum wave amplitude of the standing wave at its node. However, any asymmetries in the standing wave as in the real world would indicate asymmetries in its constituent traveling waves, and the situation would be much more complex. The nodes and antinodes in sea level can still be determined from the currents, as can the phase of the antinodes based on the directionality of the currents, but the sea level at the antinodes cannot be determined.

APPENDIX B
HFDRS

B.1 Set up and Operations

High-frequency Doppler radio scatterometer (HFDRS) maps surface currents by detecting a slow change in Bragg-scattered radio wave phase due to changes in ocean conditions. There are several types of HFDRS, but the one described here and used in this work, a WERA HFDR [Gurgel et al., 1999], is a frequency-modulated continuous wave (FMCW) beamforming HFRDS. FMCW describes the type of transmit signal used, and beamforming describes the method of angular resolution, both of which are described below.

The instrumentation of the HFDRS consists of several parts [Figure B.1]: a direct digital synthesizer (DDS) that produces a transmit (Tx) signal; a power amplifier (PA) to amplify the Tx signal; a square array of four Tx antennas to transmit the signal; a linear array of receive (Rx) antennas; receivers to filter and demodulate the Rx signals; an analog-to-digital converter (ADC) to convert the analog Rx signals to digital output; and a computer to perform digital processing.

The DDS produces a sinusoidal radio wave signal, the frequency of which changes linearly in time following a continuous saw-tooth pattern. Each little wave in frequency space is referred to as a chirp. The Tx signal is referred to by the center frequency of the chirp (e.g., a 16 MHz HFDRS has the Tx center frequency at 16 MHz), and each chirp has the same bandwidth. The Tx signal is thus continuously broadcast, and modulated in frequency, hence the designation FMCW. One copy of the Tx signal is sent to the PA, and two copies, with one phase-shifted by 90°, are sent to the local oscillator (LO) in the receiver for demodulation of Rx signals.

The PA boosts the copy of the Tx signal received from the DDS, while also band-pass filtering the Tx signal to remove any contaminating harmonics of the desired signal. The PA boosts the signal to a maximum strength of 47 dBm, or 52 W. The PA then sends the signal to the Tx antenna array. The coaxial cable through which the amplified Tx signal is sent attenuates the signal at a rate dependent on the cable type and transmit frequency [Table B.1].

The Tx antenna array is arranged in a rectangle to shape the Tx signal pattern broadcast [Figure B.2]. Two Tx antennas with $L/2$ spacing (for L the radio wavelength at the center frequency of the Tx chirp, F_c) between them form a null in the direction of their common axis. Adding another set of $L/2$ spaced antennas with $L/4$ cable delays, but with this pair $L/4$ distance from the first pair and arranged in a rectangle, will allow for a strong signal in the direction of the delayed antennas and a

null in the opposite direction. The final result is a Tx pattern with a strong signal broadcast in the direction across the common axis of the $L/4$ cable-delayed pair and away from the other antenna pair, and a null in the other three directions. The Tx antennas themselves are designed to be $L/4$ monopoles, and are tuned to be resonant at the Tx frequency.

The Rx array is located some distance from the Tx array in order to reduce the direct-path signal, or the signal received directly from the Tx antenna array. To this end, the Rx array is also ideally situated within one of the nulls created in the Tx beamforming. The linear array of Rx antennas, with each antenna being distance d from its neighbor, is situated parallel to the shoreline in order to allow for digital beamforming to take place in the computer at the end of the data-gathering process (Figure B.3). The Rx signals are also $L/4$ monopoles, tuned with a resonant frequency at the center Tx frequency. However, the spacing between the array elements here is less than $L/2$ in order to ensure the best sampling of incoming waves. The Rx signals are sent from each antenna to each receiver via a coaxial cable that again attenuates the signal.

The receivers filter the signals to remove harmonics or interference, and mix the Rx signals with the two copies of the Tx signal that are received by the LO from the DDS. The copies of the signal in the LO are those being transmitted at the time of reception; this means that there is a frequency shift between the receive signals and the demodulation signals in the LO. If the Rx signal is $\cos(F_c+\theta)$ and the LO signals are $\cos(F_c+\varphi)$ and $\sin(F_c+\varphi)$, where θ is the ocean modulation of Rx signal and φ frequency difference between Tx and Rx frequencies due to travel, then demodulation performs:

$$\cos(F_c+\varphi)\cos(F_c+\theta)=\frac{1}{2}[\cos(F_c+\varphi-F_c-\theta)+\cos(F_c+\varphi+F_c+\theta)] \qquad \text{(B.1)}$$

$$\sin(F_c+\varphi)\cos(F_c+\theta)=\frac{1}{2}[\sin(F_c+\varphi+F_c+\theta)+\sin(F_c+\varphi-F_c-\theta)] \qquad \text{(B.2).}$$

Equations (B.1) and (B.2) simplify to:

$$\cos(F_c+\varphi)\cos(F_c+\theta)=\frac{1}{2}[\cos(\varphi-\theta)+\cos(2F_c+\varphi+\theta)] \qquad \text{(B.3)}$$

$$\sin(F_c+\varphi)\cos(F_c+\theta)=\frac{1}{2}[\sin(\varphi-\theta)+\sin(2F_c+\varphi+\theta)] \qquad \text{(B.4).}$$

The demodulated signals, after analog low-pass filtering to eliminate the $2F_c$ carrier component, are sent to the ADC, which digitizes them. This leaves only the terms with the difference between Tx and Rx, and the ocean modulation. All further processing is performed digitally.

B.2 Bragg Scattering

The Tx signal is sent out over the ocean, and a signal that includes a modulation from the ocean is received by the Rx array. The Rx signal received the ocean modulation through Bragg scattering of the Tx signal off ocean surface waves. The sea state includes a broad spectrum of waves with all different wavelengths. The radio waves from the Tx array are backscattered off these waves, and are then picked up by the Rx array. The strongest signal at the Rx array will be the one that has the most constructive backscatter. In the ground-wave mode, the difference in path length for scattering off the *i*th wave versus the *i*+1 wave if waves *i* and *i*+1 having the same wavelength l, is $2l$. If these two scattered radio waves are to interfere constructively, then $2l = L$, the radio wavelength [Figure B.4]. Given the frequency range for HFDRS, Bragg scattering occurs on ocean waves of wavelength 5–50 m. Note that this is identical for classical Bragg scattering in the first-order, $\gamma = 90$ case: $2d \sin\gamma = N\Lambda$, where γ is the angle of incidence of electromagnetic radiation, d is the distance between particles in a lattice, N is the scattering order, and Λ is the wavelength of the electromagnetic radiation.

B.3 Angular Resolution

The direction from which a certain Rx signal was received is determined through a process known as beamforming. This is best explained through an inverted example: suppose planar radio waves are incident on a linear array of antennas at an angle α, from normal. If $\alpha = 0$, then the signal is received simultaneously by all Rx antennas. If $\alpha \geqslant 0$, then the signal is first received by the right-most antenna, followed by the next antenna $d \cos(90-\alpha)/c$ seconds later, where c is the speed of light. It reaches the third antenna $d \cos(90-\alpha)/c$ seconds after the second, and so on. Beamforming is "looking" in the $\beta = \alpha$ direction by adding antenna signals with the appropriate delays to isolate those signals arriving from that direction [Figure B.5].

Antenna arrays act in a manner similar to telescopes and telescope arrays in that there is a limit on the resolution of β. Telescopes have an angular resolution based on diffraction through a circular aperture:

$$\delta\beta = 1.220\frac{L}{D_a} \qquad \text{(B.5)},$$

where $\delta\beta$ is the resolution of the beamforming angle and D_a is the diameter of the circular lens of a telescope. For a telescope array, this can be approximated as:

$$\delta\beta = \frac{L}{D} \qquad \text{(B.6)},$$

where D is the antenna array length. The HFDRS RX array acts as a telescope array, with the length of Rx array. For a 16-element Rx array with a $0.45l$ spacing, this corresponds to 8° of angular resolution. However, this angular resolution is not constant in all directions. When a beam is formed at an angle, the effective antenna array length shrinks. There is thus a cosine effect to the angular resolution, with poorer resolution at larger beamforming angles [Figure B.6].

In addition, an Rx array also acts as n-slit diffraction, for n receive antennas. The intensity of n-slit diffraction is:

$$I(\beta) = I_0\left[sinc\left(\frac{\pi}{L}\sin\beta\right)\right]^2\left[\frac{\sin\left(\frac{n\pi d}{L}\sin\beta\right)}{\sin\left(\frac{\pi d}{L}\sin\beta\right)}\right]^2 \qquad \text{(B.7)},$$

where I is the signal intensity and I_0 is the base signal strength. The sinc function (or cardinal sine function, $(sinx)/x$) has side lobes, as does any Rx beamforming antenna pattern [Figure B.7]. Strong signals in the side lobes can be mapped into the main lobe during beamforming [Figure B.8].

B.4 Range Resolution

During demodulation of the Rx signal in the receiver there are two sources of frequency difference between the Rx signal and the LO signals: φ, the differences between Tx and Rx due to the frequency modulation in the DDS, and θ, the oceanic modulation. The first of these differences arises because the LO signal is received from the DDS at the same time the Rx signal arrives, so it is at a different point in the saw-tooth frequency modulation than the Rx signal is, which was sent from the DDS to the PA earlier [Figure B.9]. Because the Tx signal is a chirp, the time difference between transmission and reception of a signal is also a frequency difference between the current transmission (or LO signal) and the current reception (or Rx signal). Thus φ is a measure of the time the Rx signal spent traveling to and from the site of Bragg scattering and, also, a measure of that distance. The frequency changes linearly over a chirp, so the time between the same frequency at Rx and LO is the travel time. The actual travel time to the scattering site, one way, is one half that time, so the distance traveled at c in one half the time-difference indicated by φ is the scattering distance, or range. Sorting a single chirp into range cells via a Fourier Transform resolves range. This FT is limited in resolution by the sample time of a chirp because it is a discrete FT. The frequency resolution of φ is:

$$\delta\varphi = \frac{1}{T_c} \quad \text{(B.8)},$$

where T_c is the time period of one chirp of the Tx signal. This translates into a range resolution of:

$$\delta r = \delta\varphi\left(\frac{T_c}{B}\right) \quad \text{(B.9)},$$

where B is the bandwidth of a Tx chirp. This range resolution can be simplified into the form:

$$\delta r = \frac{c}{2\mathrm{B}}. \quad \text{(B.10)}.$$

B.5 Velocity Resolution

The demodulated and filtered Rx signals have the form $\cos(\varphi+\theta)$ and $\sin(\varphi+\theta)$. The first part of the phase, φ, changes over the course of a chirp and is used to resolve range. The second part, θ, is essentially constant within a single chirp but changes over multiple chirps. The frequency with which θ changes is dependent on the sea state at a given range and angle cell. Taking the FT of many range-resolved chirps will sort the data into a range-resolved Doppler spectrum [Figure B.10] to allow a determination of θ. The peaks in this FT for the Bragg lines, which show the most-often ascribed value of θ. θ is composed of both the surface currents and the motion of the Bragg waves, or the ocean waves on which Bragg scattering occurs. The motion of the Bragg waves is known from theory, as their speed is:

$$v_p = \sqrt{\frac{gl}{2\pi}} \quad \text{(B.11)}.$$

So the surface currents are assumed responsible for any deviation from this value.

θ is related to the velocity of the Bragg waves. Because θ is derived form a discrete FT, there is a limitation on the frequency resolution of θ [Figure B.11]:

$$\delta\theta = \frac{1}{\delta t} \quad \text{(B.12)},$$

where δt is the integration time. Normal operation of the HFDRS uses 2048 chirps in one FT; high-speed sampling uses 256, and this work uses 768:

$$\delta\theta_{256} = 12\ MHz$$

$$\delta\theta_{768} = 4\ MHz$$

$$\delta\theta_{2048} = 1.5\ MHz$$

These values can be translated into velocity resolutions by multiplying the EM wavelength as it

corresponds to a 2π phase change in one sample period:

$$\delta u = L\,\delta\theta \tag{B.13}$$

$$\delta u_{256} = 0.225\,ms^{-1}$$

$$\delta u_{768} = 0.075\,ms^{-1}$$

$$\delta u_{2048} = 0.028\,ms^{-1}$$

The data produced from processing does not come in steps as the velocity resolution would suggest. This is because the locations of the Bragg lines are determined by least-squares fitting of a Gaussian curve to the available data in the spectrum. This allows the peak of the Gaussian, and thus the determined location of the Bragg line, to fall within the gaps in the spectrum.

Table B.1. Cable attenuation in dB over 100 m for RG 213 and 1/2” Andrews Heliax over a range of commonly used HFDRS Tx frequencies.

Tx f (MHz)	Attenuation per 100 m (dB)	
	RG 213	1/2” Andrews Heliax
3	1.1	0.4
8	1.8	0.6
12	2.2	0.7
16	2.6	0.9
27	3.4	1.1

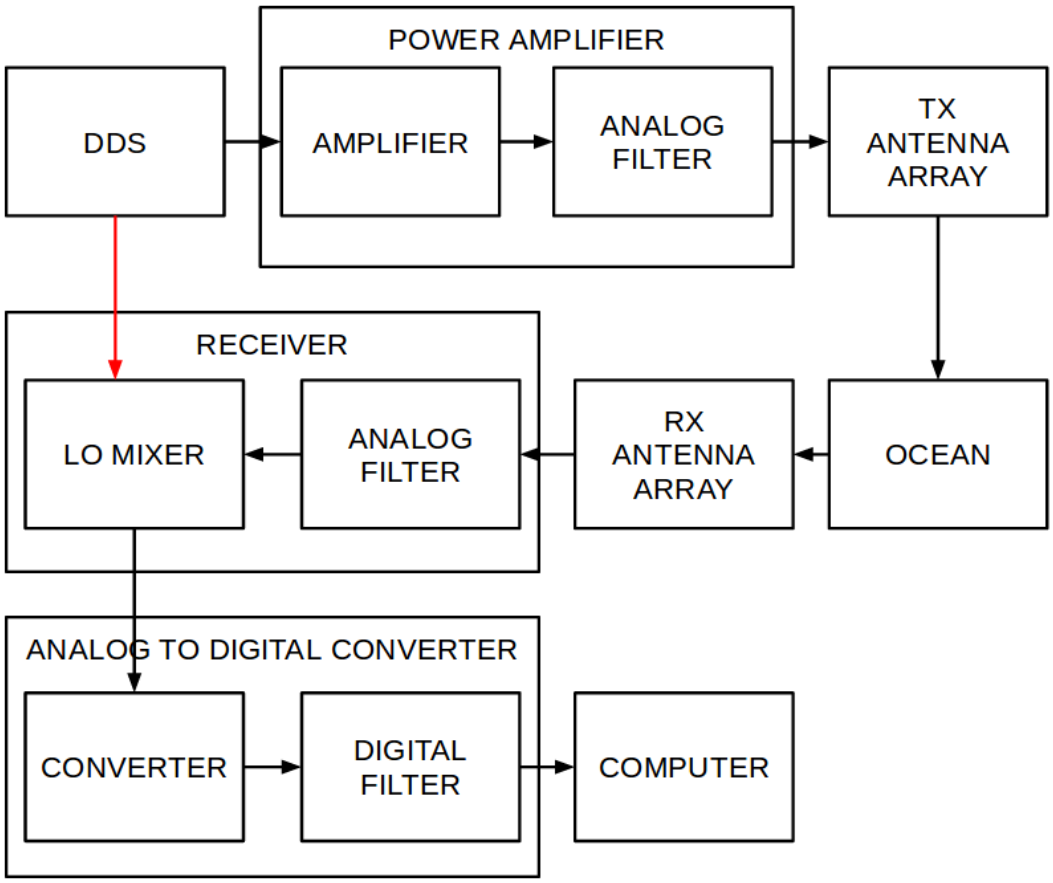

Figure B.1. Block diagram of HFDRS showing steps in chain of data-production. The red arrow represents the sine and cosine copies of the transmit signal that are sent directly to the local oscillator board in the receiver for demodulation of return signals.

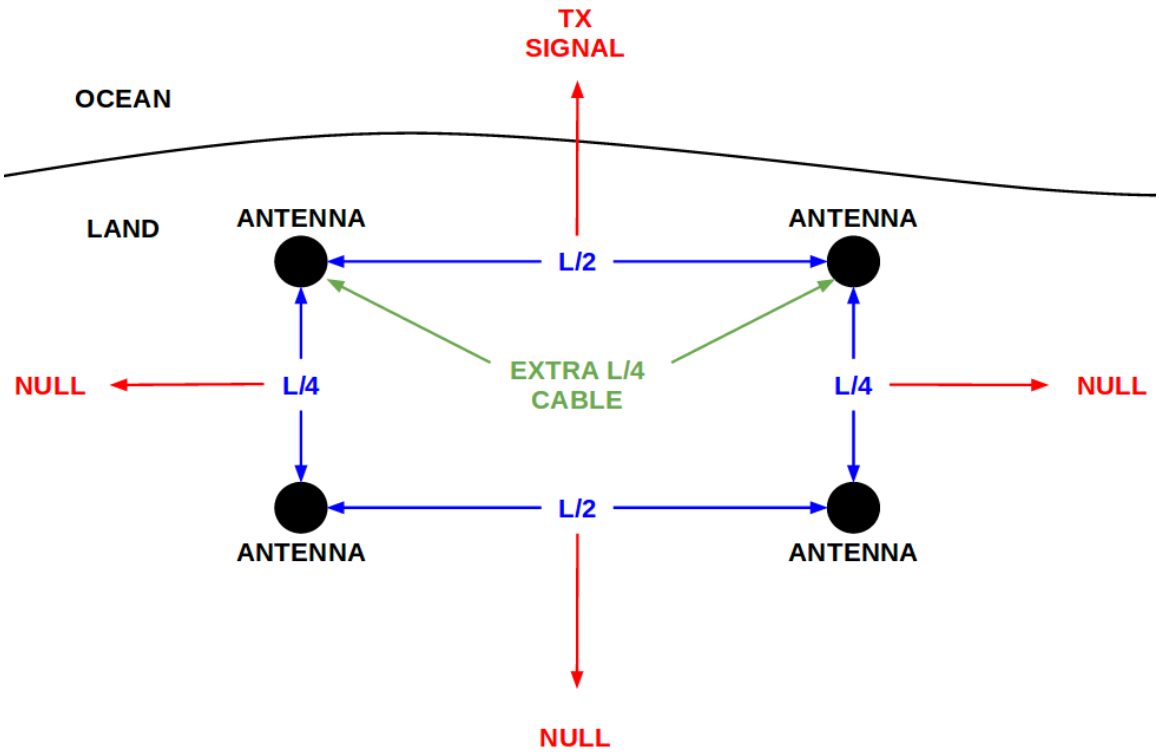

Figure B.2. Transmit antenna array showing distances between antennas, cable delays, and orientation with respect to the ocean to create three directional-nulls and amplify the signal over the ocean.

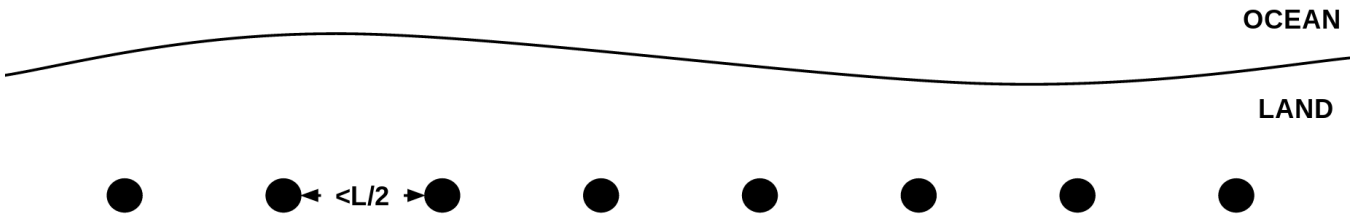

Figure B.3. Receive antenna array for HFDRS with spacing less than half the radio wavelength *L*. Array is oriented parallel to coastline.

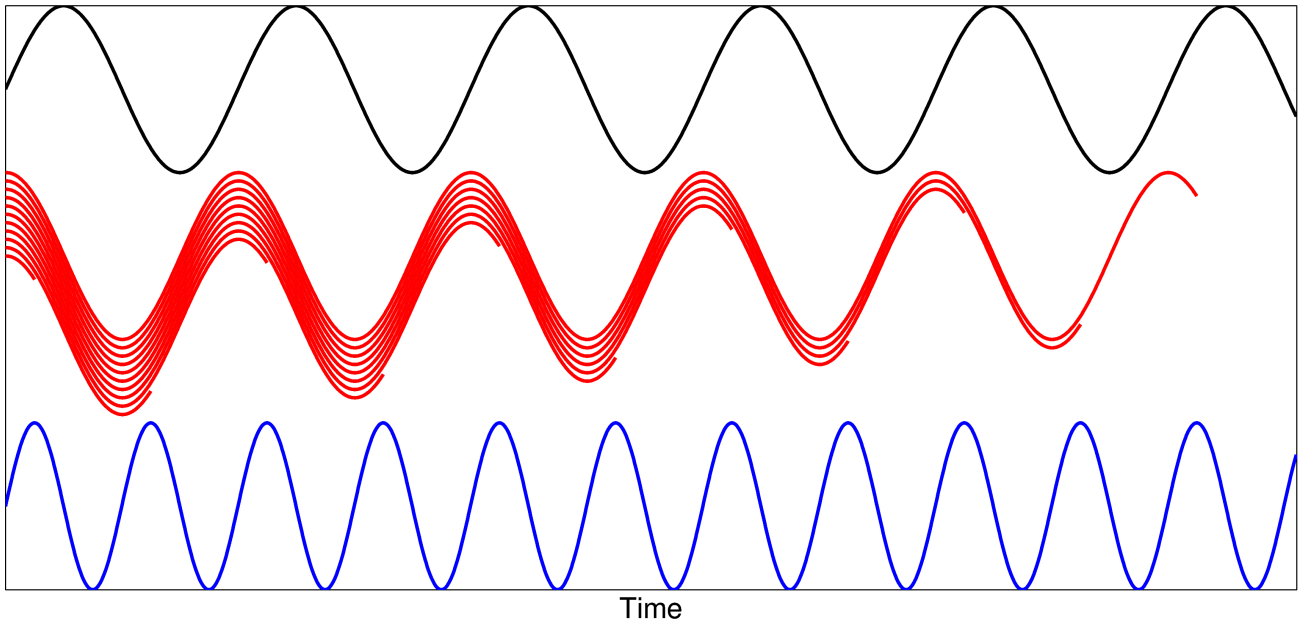

Figure B.4. Transmit signal (black) and ocean waves (blue), with Bragg scattered radio waves (red) showing that the reflected waves are in-phase with one another when the ocean wavelength *l* is one half the radio wavelength, *L*.

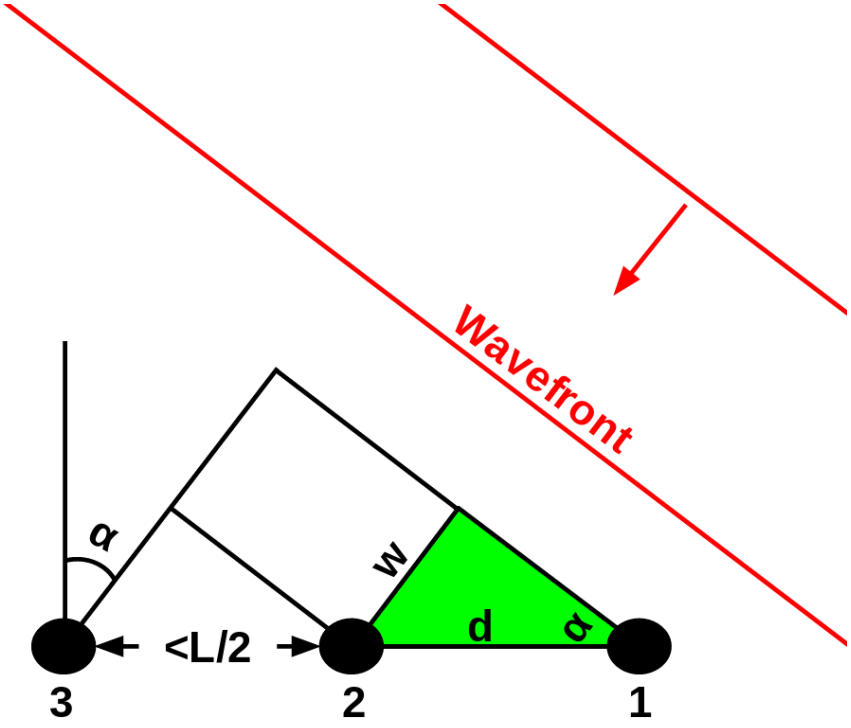

Figure B.5. Wavefronts coming towards a linear antenna array with antenna spacing *d* less than half the radio wavelength *L*, showing the extra travel distance, *w*, that results from those wavefronts arriving at an angle α relative to the normal of the antenna array. Beamforming is the process of isolating signals in one direction by taking advantage of the delay in arrival from one antenna to the next due to *w*.

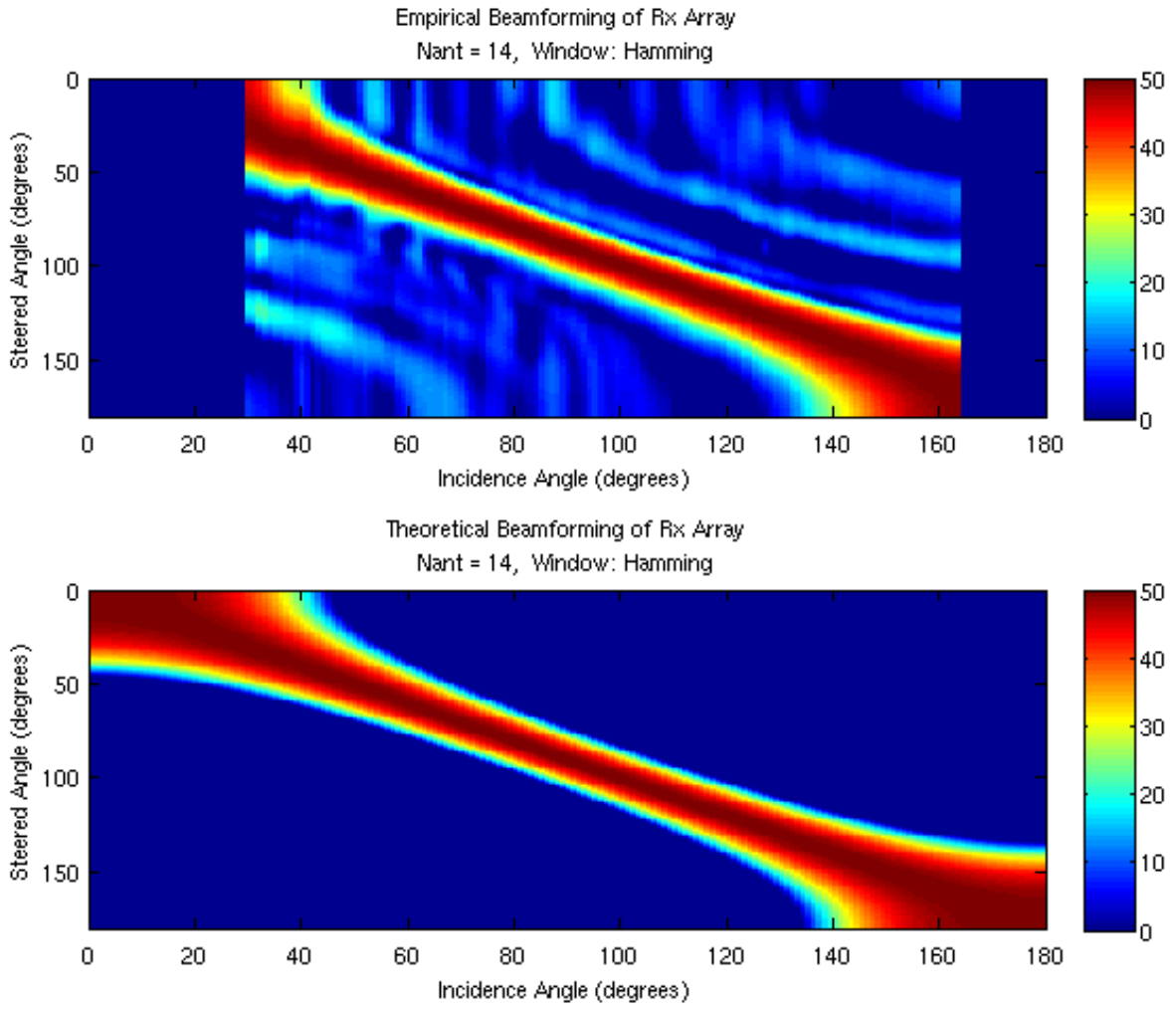

Figure B.6. Receive signal power in dB (color) for different steered angles of beamforming (y-axis) and incidence angles of signals (x-axis) for an empirical situation (top) and from theory (bottom). Notice the widening of the red color, which is the main lobe, at high angles. Also note the bands of light blue throughout the empirical plot, which are side-lobes. Courtesy of Tyson Hilmer (2011).

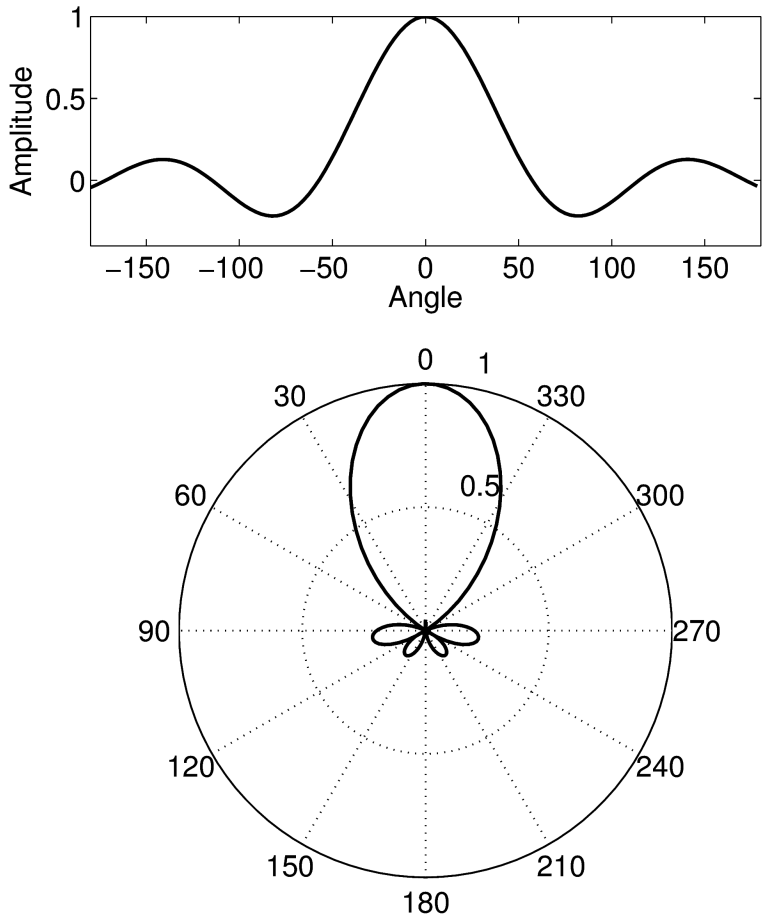

Figure B.7. Amplitude of the sinc, or cardinal sine function, with angle (top), and in a polar plot (bottom). Beamforming plots are similar because of side-lobes in intensity as a linear antenna array gives a similar intensity pattern as n-slit diffraction.

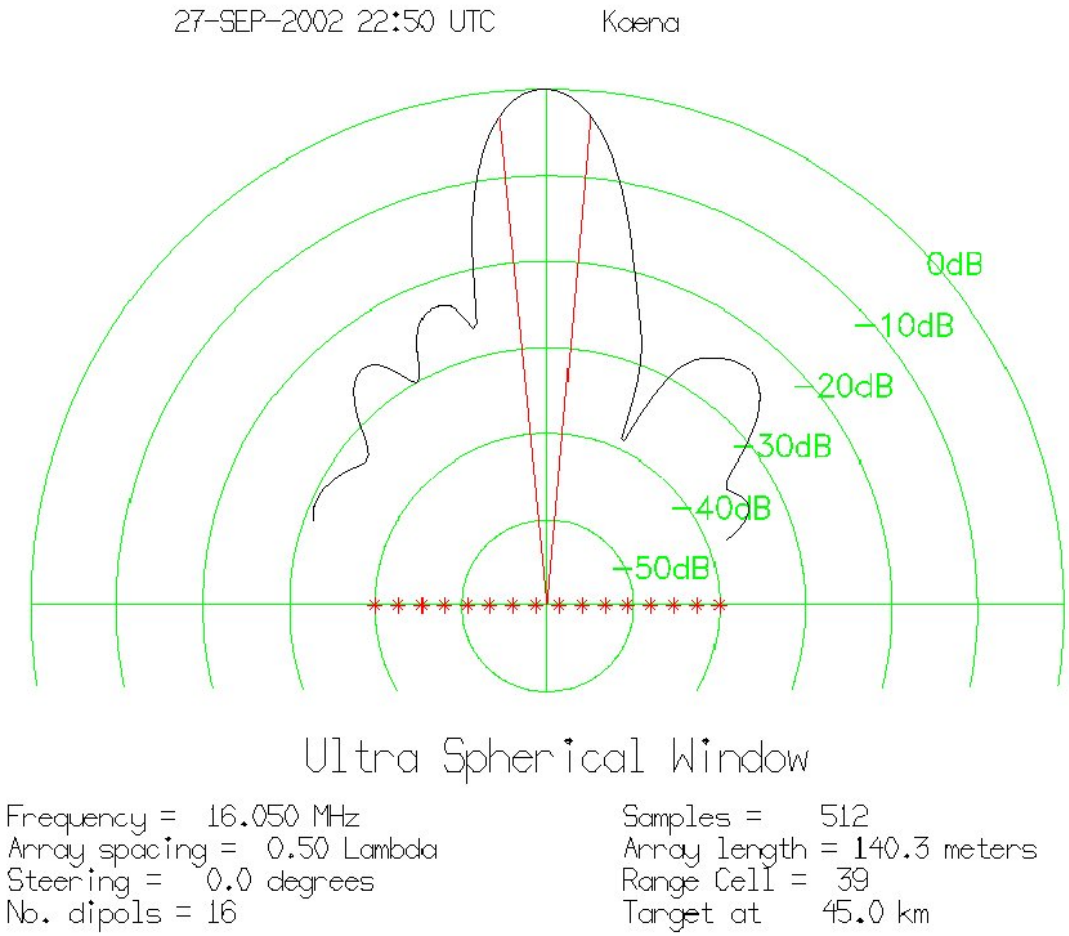

Figure B.8. Beamforming pattern from the Kaena HFDRS as an empirical example of Figure B.7, showing a main lobe and side-lobes.

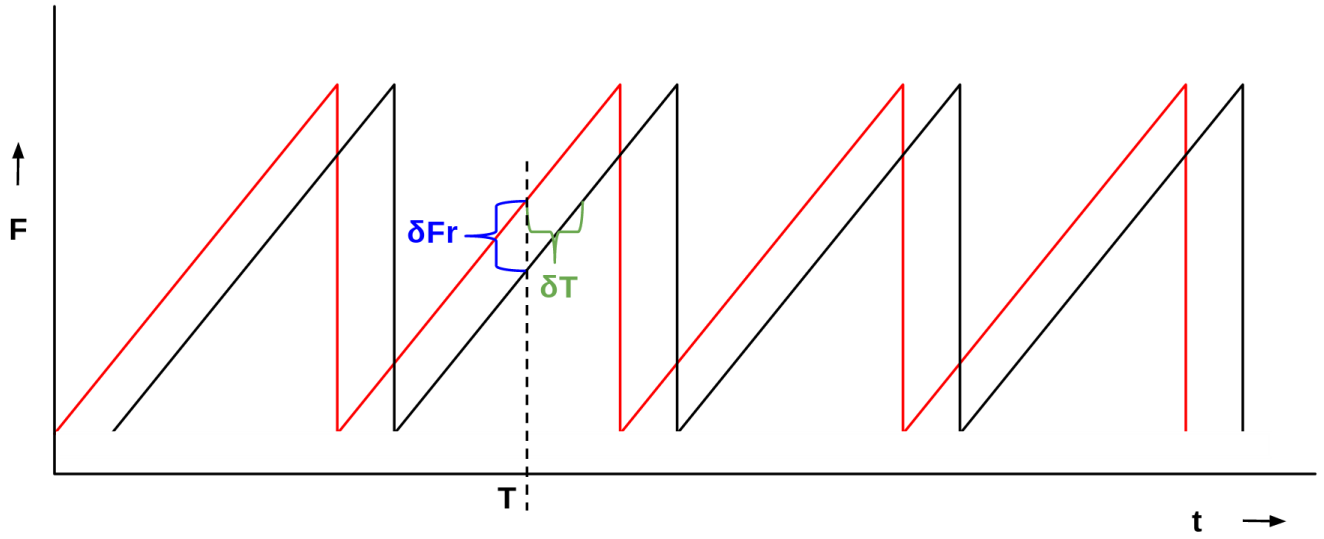

Figure B.9. Receive signal (red) and demodulation signal (black), showing chirping pattern. At time $t = T$, there is a frequency difference between the receive and demodulation signals that is proportional to a time difference due to receive signal travel, which is twice the travel time to the range of scattering. . A Fourier transform of the demodulated signal will sort the receive signals by the range.

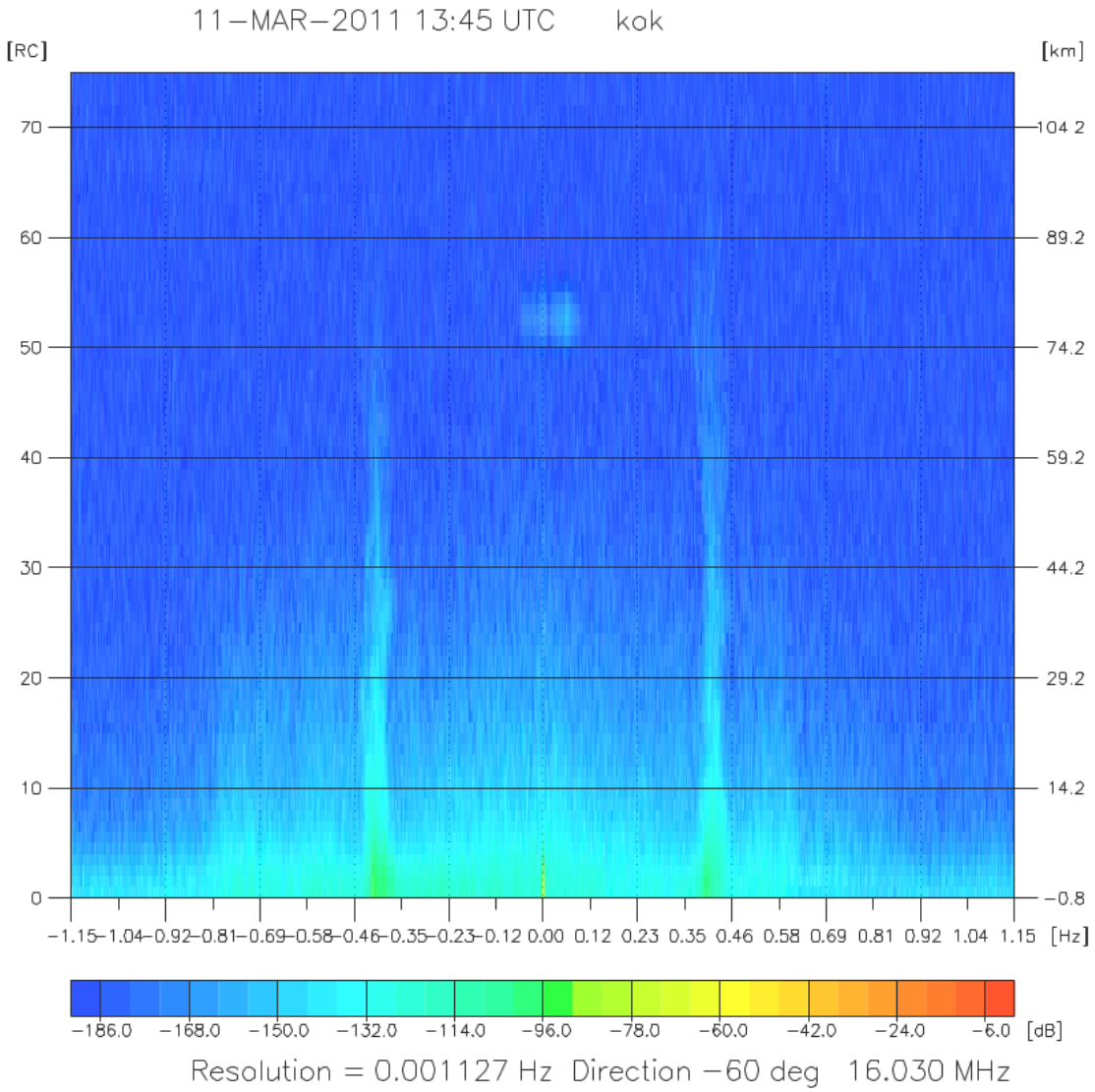

Figure B.10. Range-resolved Doppler spectrum from KOK HFDRS at 1345 UTC on 11 March 2011, during the 2011 Tohoku tsunami. The beam angle, -60º, is equivalent to 160º in the geographical sense, and runs over Penguin Bank. The two light vertical streaks are the Bragg lines, and the wavering of them at 20–40 km in range is due to currents over Penguin Bank.

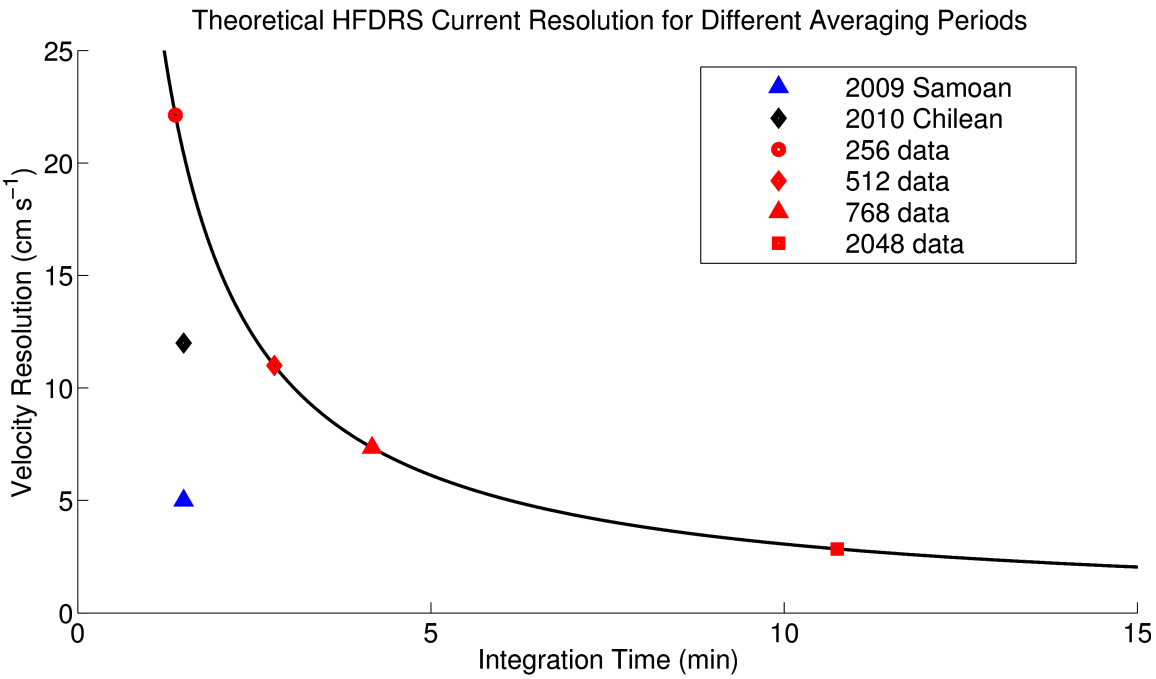

Figure B.11. Theoretical HFDRS velocity resolution for different integration times (black line) for a 16.03 MHz center frequency. The blue and black symbols represent previous tsunamis and their currents in Hawaiian waters, and the red symbols represent various integration schemes. The square, for 2048-data, is for normal KOK operation, while the triangle, 768-data, is the one used here.

APPENDIX C
METHODOLOGY

C.1 Filtering

All data was subject to zero-phase filtering twice: once with a high-pass filter with a 200 min, 3 dB cutoff to remove the tides [Figure C.1], and once with a low-pass filter with an 8.1 min, 3 dB cutoff to deal with the effects of partial overlap sampling in the HFDRS [Figure C.2].

C.2 Spectral Analysis

Spectral analysis was performed by a Fourier transform of the data with zero-padding and windowing using a Tukey window to yield the complex series ψ. The spectral amplitude, given by

$$|\psi|^2 = \Re(\psi)^2 + \Im(\psi)^2, \tag{C.1}$$

is plotted. Spectral phases are simply the argument of the spectral density, or

$$\tan^{-1}\left(\frac{\Im(\psi)}{\Re(\psi)}\right). \tag{C.2}$$

C.3 Empirical Orthogonal Function Analysis

EOF analysis was performed using the covariance method to form spatial modes as eigenvectors. These eigenvectors were then projected onto the original data set to obtain the EOF time series. The EOF maps were amplitude-normalized to one, and the normalization factor as well as the variance explained was multiplied by the EOF time series to convert the amplitudes into current magnitudes.

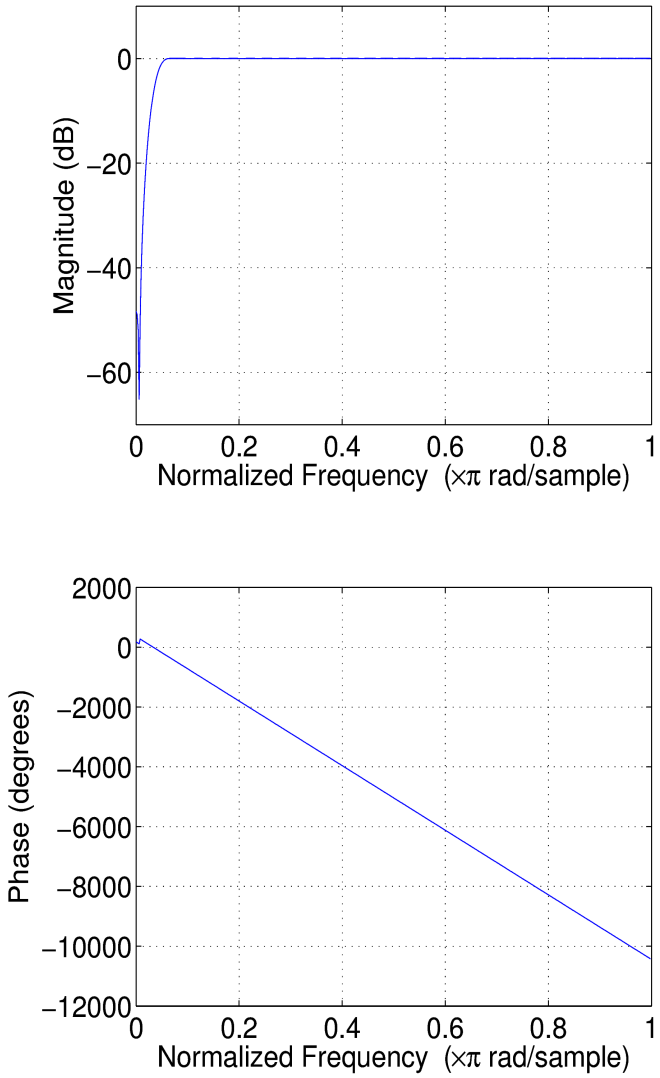

Figure C.1. High-pass FIR filter response in amplitude (top) and phase (bottom) applied to all data.

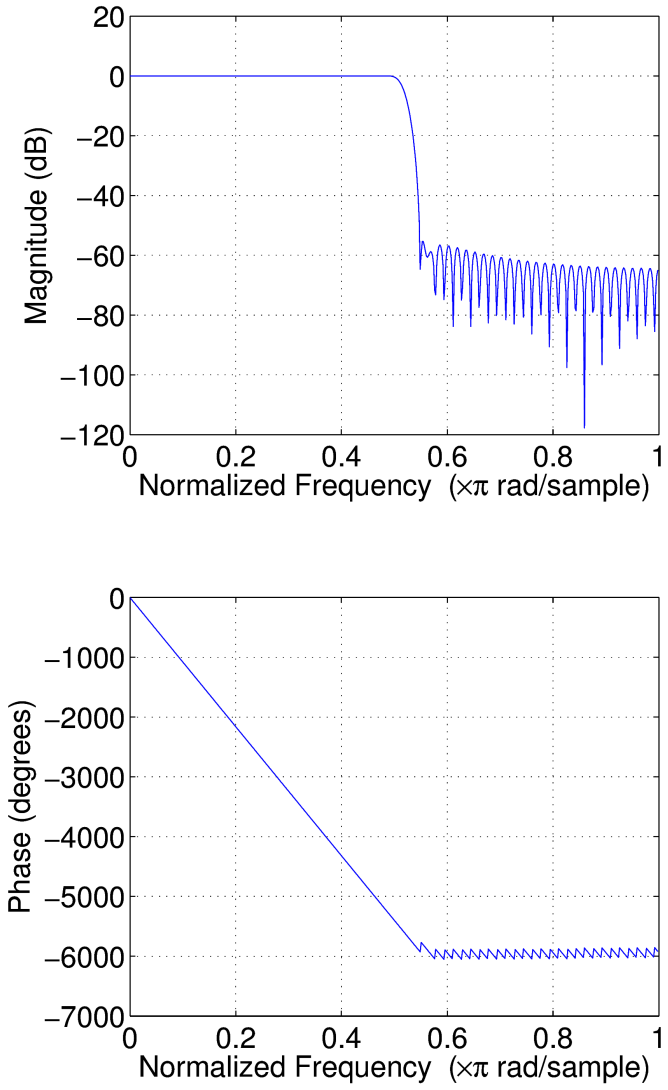

Figure C.2. Low-pass FIR filter response in amplitude (top) and phase (bottom) applied to all data.

APPENDIX D
ERROR ANALYSIS

D.1 Error of KOK Relative to Another HFDRS

HFDRS measures the surface current averaged over an area 500 m to 5 km on each side, and 0.5 m to 2 m in depth. Comparing this measurement to the top-most usable bin of an ADCP, for example, is not a comparison of like and like. However, comparison with another HFDRS is possible if there are two beams that line up against one another fairly well. Deployed on the western end of Oahu's south shore, the Kalaeloa (KAL) HFDRS operates at 16.13 MHz with the same bandwidth as KOK. It has a radial in the near-shore region that is opposite a radial of the KOK HFDRS, and a comparison of the two can give an idea of the error of KOK.

Assuming that the two HFDRS are equal and share equally the error of such a comparison, the root-mean-square error (RMSE) attributable to KOK is:

$$RMSE = \sqrt{\frac{\sum_{i=1}^{n} \left(u_{i\,KAL} - u_{i\,KOK} \right)^2}{2\mathrm{j}}} \qquad \text{(D.1)}$$

where $u_{i\,KAL}$ is the current velocity at point *i* measured by the KAL HFDRS, $u_{i\,KOK}$ is the current velocity at point *i* measured by the KOK HFDRS, and j is the number of points along the radials for comparison. When the comparison between KAL and KOK is done by this method, the error in KOK is determined to be 0.03 ms^{-1} [Figure D.1].

D.2 Spectral Analysis Error

Assuming that the time-series is normally distributed with zero mean, the Fourier transform of the data is also normally distributed with zero mean. Then both the real and imaginary parts of that transform are normally distributed with zero-mean; if they are also uncorrelated, then the spectral amplitude used here, given by Equation (C.1), is chi-squared distributed with two degrees of freedom. The windowing performed before taking the transform and spectral smoothing performed on the amplitude alters the degrees of freedom to approximately 3. The one-sigma error on the spectral amplitudes is then found from the inverse chi-squared cumulative distribution function.

D.3 Empirical Orthogonal Function Analysis

To first order, the error of an eigenvalue, or variance of an EOF, for non-degenerate modes is:

$$\delta\lambda_i \approx \lambda_i \left(2/j\right)^{1/2} \qquad \text{(D.2)}$$

where $\delta\lambda_i$ is the error on eigenvalue, or variance, λ_i and j is the number of time-steps included in

the formulation of the modes [North et al., 1982].. If there is not another eigenvalue close to λ_i, than the error of the mode is very small. If there is another eigenvalue close to λ_i, than the error of mode ξ_i is:

$$\delta\xi_i \approx \frac{\delta\lambda_i}{\Delta\lambda_i}\xi_{\hat{i}} \qquad \text{(D.3)}$$

where $\delta\xi_i$ is the error of the mode, $\Delta\lambda$ is the difference between eigenvalues for modes i and $\hat{i}$, and $\xi_{\hat{i}}$ is the value of the $\hat{i}$ mode. Essentially, if the difference between one eigenvalue and its neighbor is comparable to the error of the eigenvalue, than the error of a mode is of the order of the magnitude of the other mode. This is known as North's Rule of Thumb, from North et al. [1982].

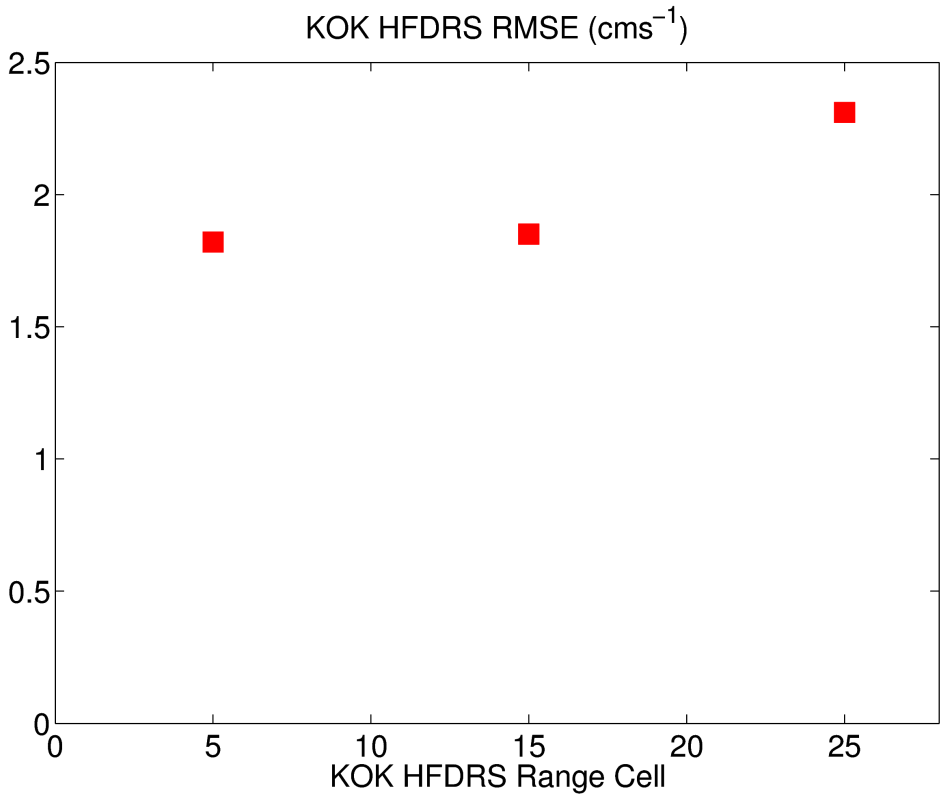

Figure D.1. Root mean square error (RMSE) of KOK HFDRS derived from comparison with KAL HFDRS.

REFERENCES

Allan, J. C., P. D. Komar, P. Ruggiero, and R. Witter (2012), The March 2011 Tohoku Tsunami and its impacts along the U.S. West Coast, *J. Coastal Res.*, 28(5), 1142–1153, doi : 10.2112/JCOASTRES-D-11-00115.1.

Barrick, D. E. (1979), A coastal radar system for tsunami warning, *Remote Sens. Environ.*, 8, 353–358, doi : 10.1016/0034-4257(79)90034-8.

Borrero, J. C., R. Bell, C. Csato, W. DeLange, D. Goring, S. D. Greer, V. Pickett, and W. Power (2013), Observations, effects, and real time assessment of the March 11, 2011 Tohoku-oki Tsunami in New Zealand, *Pure Appl. Geophys.*, 170, 1129–1248, doi : 10.1007/s00024-012-0492-6.

Bricker, J. D., S. Munger, C. Pequignet, J. R. Wells, G. Pawlak, and K. F. Cheung (2007), ADCP observations of edge waves off Oahu in the wake of the November 2006 Kuril Islands tsunami, *Geophys. Res. Lett.*, 34, L23617, doi: 10.1029/ 2007GL032015.

Cheung, K. F., Y. Bai, and Y. Yamazaki (2013), Surges around the Hawaiian Islands from the 2011 Tohoku Tsunami, *J. Geophys. Res. Oceans*, 118, 5703–5719, doi : 10.1002/jgrc.20413.

Dunbar, P., H. McCullough, G. Mungov, J. Varner, and K. Stroker (2011), 2011 Tohoku earthquake and tsunami data available from the National Oceanic and Atmospheric Administration/National Geophysical Data Center, *Geomat. Nat. Haz. R.*, 2(4), 305 – 323, doi: 10.1080/19475705.632443.

Dzvonkovskaya, A., D. Figueroa, K.-W. Gurgel, H. Rohling, and T. Schlick (2011), HF radar observation of a tsunami near Chile after the recent great earthquake in Japan, Proceedings of the 2011 International Radar Symposium (IRS), 125–130, Leipzig, Germany, Institute of Electrical and Electronics Engineers.

Gurgel, K.-W., G. Antonischki, H.-H. Essen, and T. Schlick (1999), Wellen Radar (WERA): a new ground-wave HF radar for ocean remote sensing, *Coast. Eng.*, 37, doi: 219 – 23410.1016/S0378-3839(99)00027-7.

Gurgel, K.-W., A. Dzvonkovskaya, T. Pohlmann, T. Schlick, and E. Gill (2011), Simulation and detection of tsunami signatures in ocean surface currents measured by HF radar, *Ocean Dynam.*, 61(10), 1495–1507, doi : 10.1007/s10236-011-0420-9.

Heron,M. M., A. Prytz, S. F. Heron, T. Helzel, T. Schlick, D. J. M. Greenslade, E. Schulz, and W. J. Skirving (2008), Tsunami observations by coastal ocean radar, *Int. J. Remote Sens.*, 29(21), 6347–6359, doi : 10.1080/01431160802175371.

Hinata, H., S. Fujii, K. Furukawa, T. Kataoka, M. Miyata, T. Kobayashi, M. Mizutani, T. Kokai, and

N. Kanatsu (2011), Propagating tsunami wave and subsequent resonant response signals detected by HF radar in the Kii Channel, Japan, *Estuar. Coast Shelf S.*, 95, 268–273, doi : 10.1016/j.ecss.2011.08.009.

Kaistrenko, V., N. Razjigaeva, A. Kharlamov, and A. Shishkin (2013), Manifestation of the 2011 Great Tohoku Tsunami on the coast of the Kuril Islands: a tsunami with ice, *Pure Appl. Geophys.*, 170, 1103–1114, doi : 10.1007/s00024-012-0546-9.

Kowalik, Z., J. Horrillo, W. Knight, and T. Logan (2008), Kuril Islands tsunami of November 2006: 1. Impact at Crescent City by distant scattering, *J. Geophys. Res.*, 113, C01020, doi: 10.1029/2007JC004402.

Lipa, B., D. E. Barrick, J. Bourg, and B. B. Nyden (2006), HF radar detection of tsunamis, *J. Oceanogr.*, 62, 705–716, doi : 10.1007/s10872-006-0088-9.

Lipa, B., D. Barrick, S. Saitoh, Y. Ishikawa, T. Awajii, J. Largier, and N. Garfield (2011), Japan tsunami current flows observed by HF radars on two continents, *Remote Sens.*, 3, 1663–1679, doi : 10.3390/rs3081663.

Lynett, P., R. Weiss, W. Renteria, G. D. L. T. Morales, S. Son, M. E. M. A. Arcos, and B. T. MacInnes (2013), Coastal impacts of the March 11th Tohoku, Japan tsunami in the Galapagos Islands, *Pure Appl. Geophys.*, 170, 1189–1206, doi : 10.1007/s00024-012-0568-3.

Mimura, N., K. Yasuhara, S. Kawagoe, H. Yokoki, and S. Kazama (2011), Damage from the Great East Japan Earthquake and Tsunami – a quick report, *Mitig. Adapt. Strateg. Glob. Change*, 16, 803–818, doi : 10.1007/s11027-011-9297-7.

Mori, N., T. Takahashi, T. Yasuda, and H. Yanagisawa (2011), Survey of 2011 Tohoku earthquake tsunami inundation and run-up, *Geophys. Res. Lett.*, 38, L00G14, doi : 10.1029/2011GL049210.

Munger, S., and K. F. Cheung (2008), Resonance in Hawaii waters from the 2006 Kuril Islands Tsunami, *Geophys. Res. Lett.*, 35, L07605, doi : 10.1029/007GL032843.

National Police Agency of Japan (NPAJ), Emergency Disaster Countermeasures Headquarters, Damage Situation and Police Countermeasures associated with 2011 Tohoku district - off the Pacific Ocean Earthquake, (http://www.npa.go.jp/archive/keibi/biki/higaijokyo_e.pdf), Retrieved 10 June 2014.

North, G. R., T. L. Bell, R. F. Cahalan, and F. J. Moeng (1982), Sampling errors in the estimation of empirical orthogonal functions, *Mon. Wea. Rev.*, 110, 699–706, doi: 10.1175/1520-0493(1982)110<0699:SEITEO>2.0.CO;2.

Pacific Tsunami Warning Center (PTWC), Tsunami message archive, ptwc.weather.gov/ptwc.archive.php.

Roeber, V., Y. Yamazaki, and K. F. Cheung (2010), Resonance and impact of the 2009 Samoa tsunami around Tutuila, American Samoa, *Geophys. Res. Lett.*, 37, L21604, doi : 10.1029/2010GL044419.

Song, Y. T., I. Fukumori, C. K. Shum, and Y. Yi (2012), Merging tsunamis of the 2011 Tohoku-Oki earthquake detected over the open ocean, *Geophys. Res. Lett.*, 39, L05606, doi : 10.1029/2011GL050767.

Tsai, V. C., J.-P. Ampuero, H. Kanamori, and D. J. Stevenson (2013), Estimating the effect of Earth elasticity and variable water density on tsunami speeds, *Geophys. Res. Lett.*, 40, 492–496, doi: 10.1002/grl.50147.

Watada, S. (2013), Tsunami speed variations in density-stratified compressible global oceans, *Geophys. Res. Lett.*, 40, 4001–4006, doi : 10.1002/grl.50785.

Yamazaki, Y., and K. F. Cheung (2011), Shelf resonance and impact of near-field tsunami generated by the 2010 Chile earthquake, *Geophys. Res. Lett.*, 38, L12605, doi : 10.1029/2011GL047508.

Yamazaki, Y., K. F. Cheung, and Z. Kowalik (2011a), Depth-integrated, non-hydrostatic model with grid nesting for tsunami generation, propagation, and run-up, *Int. J. Numer. Meth. Fluids*, 67(12), 2018–2107, doi : 10.1002/fld.2485.

Yamazaki, Y., K. F. Cheung, G. Pawlak, and T. Lay (2012), Surges along the Honolulu coast from the 2011 Tohoku tsunami, *Geophys. Res. Lett.*, 39, L09604, doi : 10.1029/2012GL051624.

Yamazaki, Y., T. Lay, K. F. Cheung, H. Yue, and H. Kanamori (2011b), Modeling near-field tsunami observations to improve finite-fault slip models for the 11 March 2011 Tohoku earthquake, *Geophys. Res. Lett.*, 38, L00G15, doi : 10.1029/2011GL049130.

Yamazaki, Y., Z. Kowalik,and K. F. Cheung (2009), Depth-integrated, non-hydrostatic model for wave breaking and run-up, *Int. J. Numer. Meth. Fluids*, 61(5), 473–497, doi : 10.1002/fld.1952.